

Article

Synthesis of New Organoselenium-Based Succinanic and Maleanilic Derivatives and In Silico Studies as Possible SARS-CoV-2 Main Protease Inhibitors

Saad Shaaban ^{1,2,*}, Yasair S. Al-Faiyz ¹, Ghayah M. Alsulaim ^{1,*} , Mohamed Alaasar ^{3,4}, Nasser Amri ⁵, Hussein Ba-Ghazal ¹, Ahmed A. Al-Karmalawy ⁶  and Aly Abdou ^{7,*} 

¹ Department of Chemistry, College of Science, King Faisal University, Al-Ahsa 31982, Saudi Arabia; yalfaiz@kfu.edu.sa (Y.S.A.-F.); hbaghazal@kfu.edu.sa (H.B.-G.)

² Department of Chemistry, Faculty of Science, Mansoura University, Mansoura 35516, Egypt

³ Institute of Chemistry, Martin Luther University Halle-Wittenberg, 6099 Halle/Saale, Germany; mohamed.alaasar@chemie.uni-halle.de

⁴ Department of Chemistry, Faculty of Science, Cairo University, Giza 12566, Egypt

⁵ Department of Chemistry, Faculty of Science, Jazan University, Jazan 45142, Saudi Arabia; namri@jazanu.edu.sa

⁶ Pharmaceutical Chemistry Department, Faculty of Pharmacy, Ahram Canadian University, 6th of October City, Giza 12566, Egypt; akarmalawy@acu.edu.eg

⁷ Department of Chemistry, Faculty of Science, Sohag University, Sohag 82524, Egypt

* Correspondence: sbrahim@kfu.edu.sa (S.S.); g.m.alsulaim@gmail.com (G.M.A.);

aly_abdou@science.sohag.edu.eg (A.A.)

Abstract: Herein we report the synthesis of organic selenide-based maleanilic and succinanic acids in good yields (up to 95%). Their structural identities were elucidated by spectroscopic techniques (e.g., IR, ¹H- & ¹³C-NMR, and MS). The ADMET analysis, molecule electrostatic potential map, DFT, and frontier molecular orbital were used to study the organoselenium compounds' pharmacokinetics, drug-likeness characteristics, geometries, and chemical and electronic properties. Moreover, a molecular docking tool was employed to investigate the organic selenides' ability to inhibit the SARS-CoV-2 Mpro target (PDB: 7BFB). Within this context, organic selenides exhibited promising binding affinities to the SARS-CoV-2 Mpro receptor in the following order (12 > 11 > 10 > 9 > 7 > 8). Furthermore, molecular dynamics simulations were also carried out for 200 ns to evaluate the exact behavior of the most active compound (12) within the M^{PRO} binding pocket of SARS-CoV-2 compared with its co-crystallized inhibitor (Co).

Keywords: organic selenides; selenium; maleic; succinic; in silico; SARS-CoV-2



Citation: Shaaban, S.; Al-Faiyz, Y.S.; Alsulaim, G.M.; Alaasar, M.; Amri, N.; Ba-Ghazal, H.; Al-Karmalawy, A.A.; Abdou, A. Synthesis of New Organoselenium-Based Succinanic and Maleanilic Derivatives and In Silico Studies as Possible SARS-CoV-2 Main Protease Inhibitors. *Inorganics* **2023**, *11*, 321. <https://doi.org/10.3390/inorganics11080321>

Academic Editor: Bruno Therrien

Received: 16 June 2023

Revised: 25 July 2023

Accepted: 26 July 2023

Published: 29 July 2023



Copyright: © 2023 by the authors. Licensee MDPI, Basel, Switzerland. This article is an open access article distributed under the terms and conditions of the Creative Commons Attribution (CC BY) license (<https://creativecommons.org/licenses/by/4.0/>).

1. Introduction

Selenium-based organic scaffolds have acquired particular interest owing to their numerous applications in medicinal and material chemistry and the unique characteristics of the selenium element [1]. The latter is found in nearly all organisms in the form of selenoenzymes such as the thioredoxin reductases (TrxR), deiodinase, and glutathione peroxidase (GPX) [2]. Furthermore, selenium is important in the human defense system against oxidative stress and oxidative damage [3]. Therefore, it is also of fundamental interest for the immune system's regular action, which tolerates viral infection resistance. In other respects, a lack of selenium was correlated with the progression of viral infection and severity of diseases [4]. Furthermore, selenium enhances host immunity by stimulating the TrxR and GPX activities and modulating the redox levels.

Selenium is characterized by its larger size, lower electronegativity, and higher polarizability than the sulfur atom [5]. Therefore, several organoselenium (OSe) compounds were reported to exhibit good catalytic activity and to suppress oxidative-stress-related syndrome progression via scavenging reactive oxygen and nitrogen-free radicals [6]. Moreover,

in materials science, some of the OSe agents are used in hydrogen production, photovoltaic cells, and sodium-ion batteries due to their semiconductor potential [6,7].

Selenium is found in various naturally occurring and pharmaceutically active synthetic agents (Figure 1). For example, in selenoamino acids such as selenomethionine (I), selenocysteine (II) [8], or inethaselen (III) [9], which manifested good TrxR inhibition activity and recently reached a stage II clinical trial. One class of the most studied OSe compounds is ebselen (IV), which is characterized by its viral inhibition potency for different microbes such as Zika, hepatitis C, influenza A, and human immunodeficiency viruses and its good GPX-like activity. It has been used for the treatment of bipolar disorders such as hypo/manic syndromes (Figure 1) [10,11].

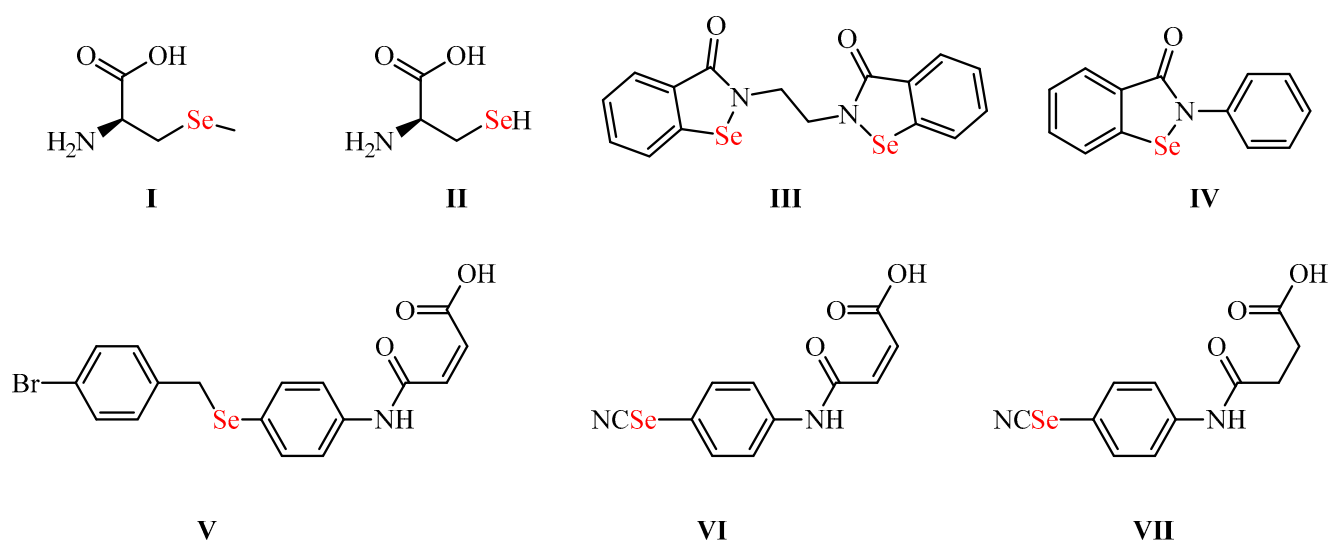


Figure 1. Important organoselenium agents (I–VII) with diverse applications.

Harrison and Sachs (2022) state that the origin of the virus is still unclear and that there are two main hypotheses: natural spillover from animals to humans or accidental escape from a laboratory. Their document also claims that there is evidence for both scenarios and that an independent inquiry is needed to resolve this issue and prevent future pandemics [12].

Mpro inhibitors are molecules that can block the activity of the main protease (Mpro) of SARS-CoV-2, the virus that causes COVID-19. Mpro is an enzyme that helps the virus to replicate and infect cells, so inhibiting it could be a potential strategy to treat COVID-19. Some of the Mpro inhibitors that have been studied include natural and synthetic compounds. These inhibitors have been shown to bind to the Mpro and reduce its flexibility, which is important for its catalytic function [13,14].

Although the SARS-CoV-2 main protease is a model therapeutic target, no medication can be administered for this condition [15–17]. The papain-like protease (PL^{P_{ro}}) and the major protease (M^{P_{ro}}) play an essential part in the reproduction of the virus [18,19]. Li and Kang underlined that these major proteases are encoded by the viral genome and might be a promising therapeutic target since they are crucial in splitting viral polyproteins into functional proteins [20]. Therefore, inhibiting these key proteases is promising for developing novel anti-COVID drugs [17].

A recent high-throughput screening study by Jin et al. [18,21] identified ebselen as a promising antiviral agent among more than 10,000 candidates as a lead inhibitor of M^{P_{ro}} [18,22]. Within this context, the antiviral activity of ebselen suggested the promise of OSe agents as possible M^{P_{ro}} inhibitors by interaction with the virus infection cycle [23,24]. Ebselen can efficiently bind to the cysteine located in the M^{P_{ro}} active site, thus forming selenosulfide, which causes the inactivation of the virus with an IC₅₀ = 0.67 μM [22,23,25].

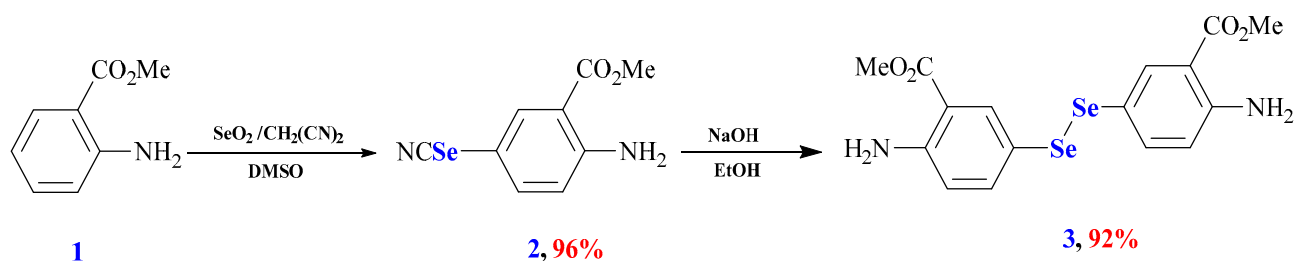
In accordance with the above, several groups have made significant progress either in the development of seleno-organic compounds with potential antiviral activities or via studying their mechanisms [18,19].

N-maleamic and *N*-succinamic acids represent key building blocks in organic synthesis [26–29]. Owing to their stability and reactivity, they are used for synthesizing natural products, functionalized polymers, and peptides [28–30]. In addition, they are also involved in various industrial applications, including rubber, adhesives, resins, optoelectronics, and aerospace [26,28–30]. Recently, we have developed different OSe-based *N*-maleanilic and *N*-succinamic acids (V–VII) with exciting anti-apoptotic, antioxidant, and anticorrosive activities [31]. Inspired by these findings, we describe novel OSe-based *N*-maleanilic and *N*-succinamic acids. Furthermore, the synthesized organic selenides were investigated for their chemical and electronic activities, drug-likeness, and pharmacokinetic properties using different techniques, including density function theory (DFT), molecule electrostatic potential maps, frontier molecular orbitals, and ADMET analysis. Moreover, molecular docking and molecular dynamics simulations were performed to propose the potential anti-SARS-CoV-2 activity of the newly synthesized OSe candidates as well.

2. Results and Discussion

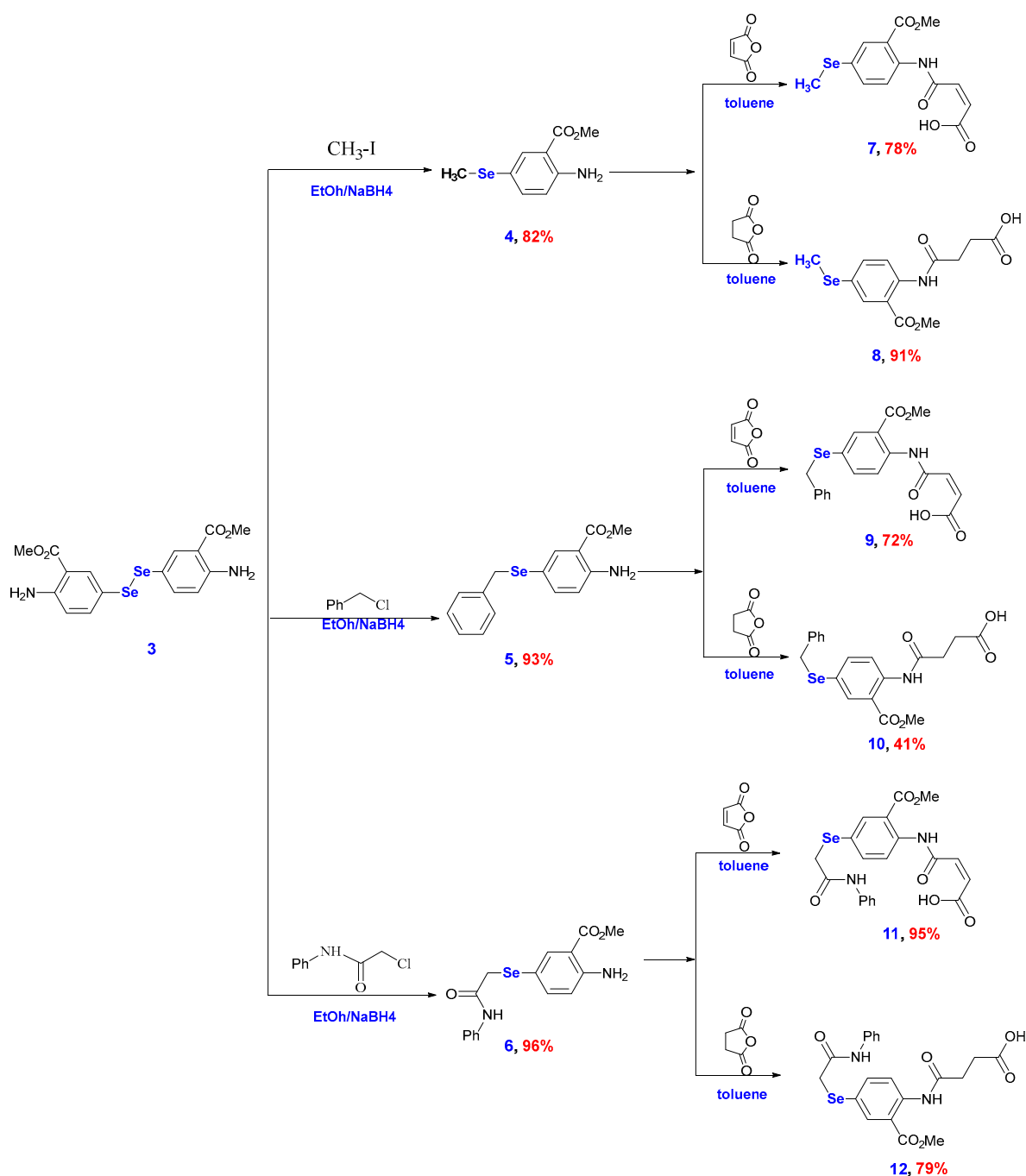
2.1. Chemistry

The synthesis of OSe agents is usually accompanied by various synthetic difficulties, such as using expensive and toxic reagents (e.g., NaSeH, KSeCN, Na₂SeSO₃, and Cu₂Se) [5]. On the other hand, the design and synthetic strategies of the OSe compounds rely on their skeleton natures (e.g., selenocyanates and diselenides) [5–7]. The synthesis of the target materials in the current work was started by synthesizing compound **2**, which obtained 96% yield via the selenocyanation of methyl anthranilate using selenium dioxide and malononitrile (Scheme 1) [32]. The alkaline hydrolysis of **2** furnished the diaryldiselenide **3** in 92% yield (Scheme 1), which was used as an intermediate to synthesize the final products [32].



Scheme 1. Synthesis of organoselenium agents **2** and **3**. Reagents and conditions: (i) methyl anthranilate (6.25 mmol), $\text{CH}_2(\text{CN})_2$ (7.5 mmol), SeO_2 (15 mmol), and DMSO (5 mL), 30 min, RT; (ii) compound **2** (2 mmol), NaOH (2 mmol), and anhydrous ethanol (10 mL), 90 min, RT.

The reduction of the diaryldiselenide **3** using NaBH_4 afforded the corresponding sodium selenate (generated in situ), which is a strong nucleophile. The reaction of this nucleophile with different alkyl halides, namely CH_3I , PhCH_2Cl , and $\text{PhNHCOCH}_2\text{Cl}$ affords the corresponding selenide-based methyl anthranilates **4**, **5**, and **6** in 82%, 93%, and 96% yields, respectively [32]. Maleoylation and succinylation of the OSe primary aromatic amines **4**, **5**, and **6** with maleic and succinic anhydrides give the maleanilic **7**, **9**, and **11** and succinamic **8**, **10**, and **12** derivatives in 78%, 91%, 72%, 41%, 95%, and 79% yields, respectively (Scheme 2).



Scheme 2. Preparation of OSe acids 7–12. Reagents and conditions: (i) reduction of diaryl diselenide **3** with NaBH_4 followed by a nucleophilic substitution reaction with different alkyl halides in anhydrous ethanol at RT for 90 min; (ii) amines **4**, **5**, or **6** (1 mmol), maleic or succinic anhydride (1.3 mmol), and methylbenzene (3 mL), at RT for 90 min.

The ^1H NMR spectra of the synthesized maleanilic acids showed the characteristics of doublet signals for the olefinic protons ($\text{HC}=\text{CH}$) at 6.54 ppm and 6.35 ppm for compound **7**, at 6.54 ppm and 6.32 ppm for compound **9**, and at 6.59 ppm and 6.36 ppm for compound **11**. Furthermore, these olefinic protons' J coupling constant values were 12.4, 12.4, and 8.5 Hz, respectively. Therefore, the Z isomer is the most probable configuration for compounds **7**, **9**, and **11**. These results follow our previous reports where the N-maleanilic acids, namely (Z)-4-((4-((4-bromobenzyl)selenyl)phenyl)amino)-4-oxobut-2-enoic acid, (Z)-4-((4-((4-bromobenzyl)selenyl)phenyl)amino)-4-oxobut-2-enoic acid, and (Z)-4-((4-((3-methyl-

1,4-dioxo-1,4-dihydronaphthalen-2-yl) selanyl)phenyl)amino)-4-oxobut-2-enoic acid also showed similar J coupling constant values at 12, 12.1, and 12.1 Hz for their olefinic protons, respectively [20,25].

On the other hand, the ^1H NMR spectra of the succinanilic acids showed the characteristic triplet signals for the two vicinal methylene groups ($\text{CH}_2\text{-CH}_2$) at 2.60 ppm and 2.55 ppm for compound **8**, at 2.61 ppm and 2.53 ppm for compound **10**, and at 2.62 ppm and 2.53 ppm for compound **12**. Furthermore, the methyl groups (SeCH_3) attached to the Se atom appeared as singlet signals at 2.37 ppm and 2.38 ppm for compounds **7** and **8**, respectively. Furthermore, the singlet signals of the CH_2 groups (SeCH_2) attached to the Se atom in compounds **9**, **10**, **11**, and **12** appeared at 4.26 ppm, 4.22 ppm, 3.74 ppm, and 3.72 ppm, respectively (see the experimental part and supporting information for the NMR copies).

Moreover, compounds **7–12** are trisubstituted-1,2,4-benzene; therefore, the three aromatic protons were nonequivalent. The proton with no ortho proton (the lone proton) appeared doublet. The proton para to the lone proton is coupled only with the proton ortho to it and shows as a doublet signal, and the third proton ortho and meta to its neighbors exhibited a characteristic ortho/meta doublet of doublets signal.

The ^{13}C NMR of the maleanilic acids showed two distinctive aliphatic carbon signals at 52.46 ppm and 7.00 ppm for compound **7**, at 52.44 ppm and 31.10 ppm for compound **9**, and at 52.43 ppm and 30.77 ppm for compound **11**. In the case of succinanilic acids, four aliphatic carbon signals appeared at 52.39 ppm, 31.59 ppm, 28.68 ppm, and 7.07 ppm for compound **8**, at 52.35 ppm, 31.67 ppm, 31.16 ppm, and 28.58 ppm for compound **10**, and at 52.51 ppm, 31.89 ppm, 30.99 ppm, and 28.76 ppm for compound **12**. Moreover, compounds **7**, **8**, **9**, and **10** showed three distinctive downfield carbonyl carbons (C=O) ($\sim 173\text{--}163$ ppm), whereas compounds **11** and **12** showed four distinctive downfield carbonyl carbons (C=O) ($\sim 173\text{--}163$ ppm) (see the experimental part and supporting information for the NMR copies).

2.2. DFT Calculations

The density functional theory (DFT) is one of the most common quantum chemistry methods used for quantitative prediction and explanation of the mode of action of biomolecules [33]. Therefore, DFT investigations were performed for the new materials. Furthermore, the highest occupied molecular orbital (HOMO) and the lowest unoccupied molecular orbital (LUMO) were used to evaluate the energy gap ($\Delta E = E_{\text{LUMO}} - E_{\text{HOMO}}$), electron affinity (E.A. = $-E_{\text{LUMO}}$), ionization potential (I.P. = $-E_{\text{HOMO}}$), electronegativity ($\chi = (\text{I.P.} + \text{E.A.})/2$), chemical potential ($\text{cp} = -\chi$), chemical hardness ($\eta = (\text{I.P.} - \text{E.A.})/2$), softness ($\sigma = 1/\eta$), and electrophilicity index ($\omega = \chi^2/2\eta$) [34,35].

2.2.1. Conformational Analysis

The energies were calculated for the various generated conformers using the B3LYP method with a 6-311G (d, p) basis set to find the most optimized geometry. The computationally predicted different possible conformers obtained and the total energies are shown and listed in Figure S1 (see supporting information). The structure optimizations have demonstrated that the conformers of the C1 of compound **7**, C3 of compound **8**, C3 of compound **9**, C9 of compound **10**, C3 of compound **10**, and C9 of compound **12** produced the minimum global energy. Therefore, conformers C1, C3, C3, C9, C3, and C9 form the most stable conformers of compounds **7**, **8**, **9**, **10**, **11**, and **12**, respectively. Furthermore, the frequency calculations based on the B3LYP method with a 6-311G (d, p) basis set confirm the compounds' stability, as the obtained molecules do not have any imaginary frequencies.

2.2.2. Geometry Optimization

Molecular modeling is a fundamental approach for the structural analysis of ligand templates, as it offers additional structural details and energy-minimized conformation [36].

Therefore, applying the 6–311 (d, p) basis set, the final compounds (7–12) were investigated, and the optimized confirmations are shown in Figure 2.

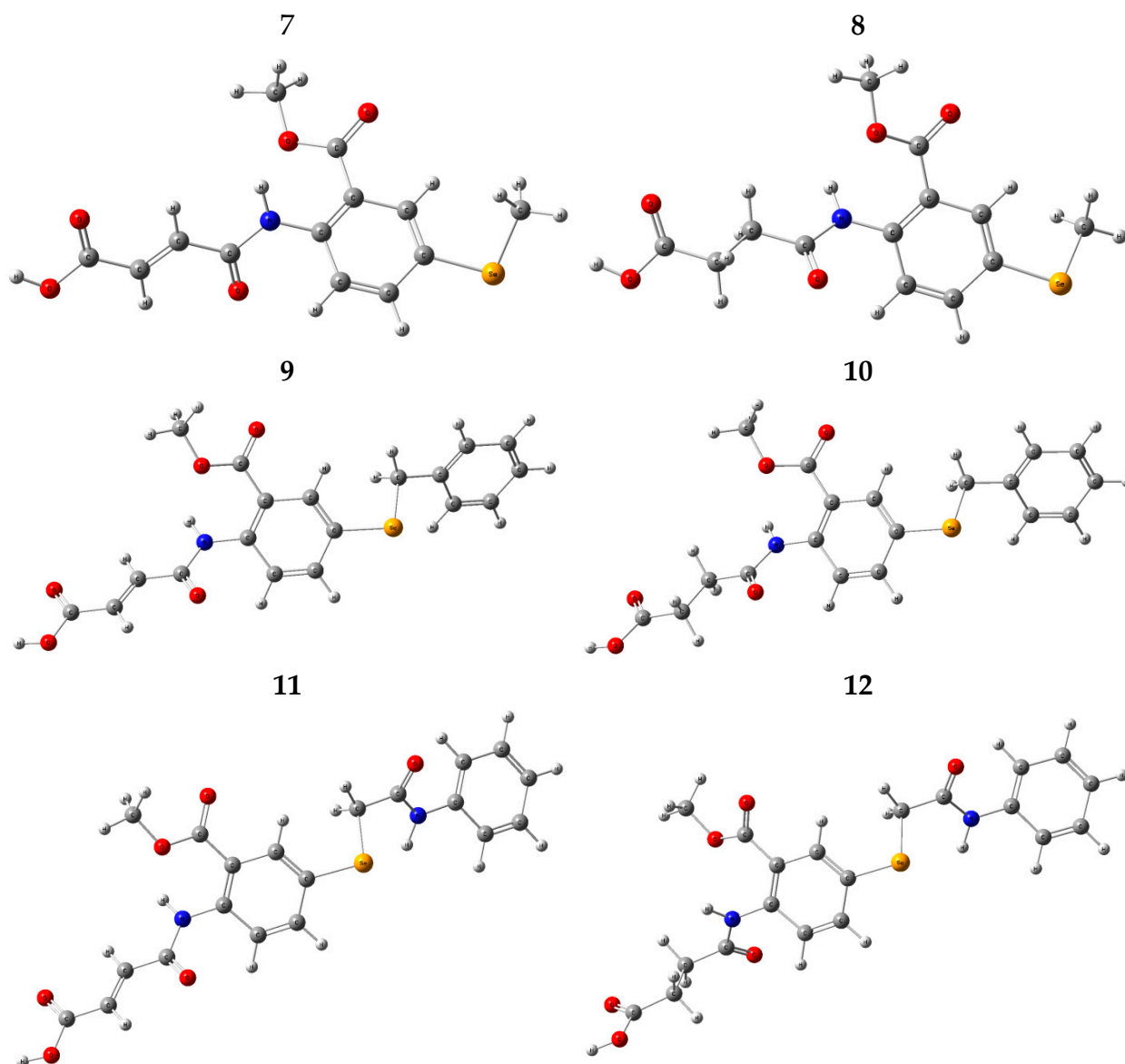


Figure 2. Optimized confirmations with atom labels using DFT/B3LYP.

2.2.3. Frontier Molecular Orbital (FMO) Analysis

Orbital analysis allows chemists to understand chemical processes better. Therefore, molecular orbitals (MOs) are essential for a deeper understanding of chemical processes and electronic properties. In 1952, Fukui introduced the frontier orbital theory, which connects the properties of the HOMO (highest occupied molecular orbital) and LUMO (lowest unoccupied molecular orbital) with reactivity [37,38]. Figure 3 shows a sketch of the molecular orbital diagrams for the HOMO and LUMO states of the final compounds (7–12).

DFT calculations can predict the pharmacological potency of compounds using key activity parameters derived from the E_{HOMO} and E_{LUMO} energies, as shown in Figure 3 [39,40]. This is because the electrons are primarily distributed over the molecule. As a result, various parameters such as the energy gap (ΔE , eV), ionization potential (I.P., eV), electron affinity (E.A., eV), electronegativity (χ , eV), chemical potential (cp, eV), chemical hardness (η , eV), chemical softness (σ , eV^{-1}), and electrophilicity index (ω , eV) can be estimated using LUMO–HOMO energies [39,40] (Table 1).

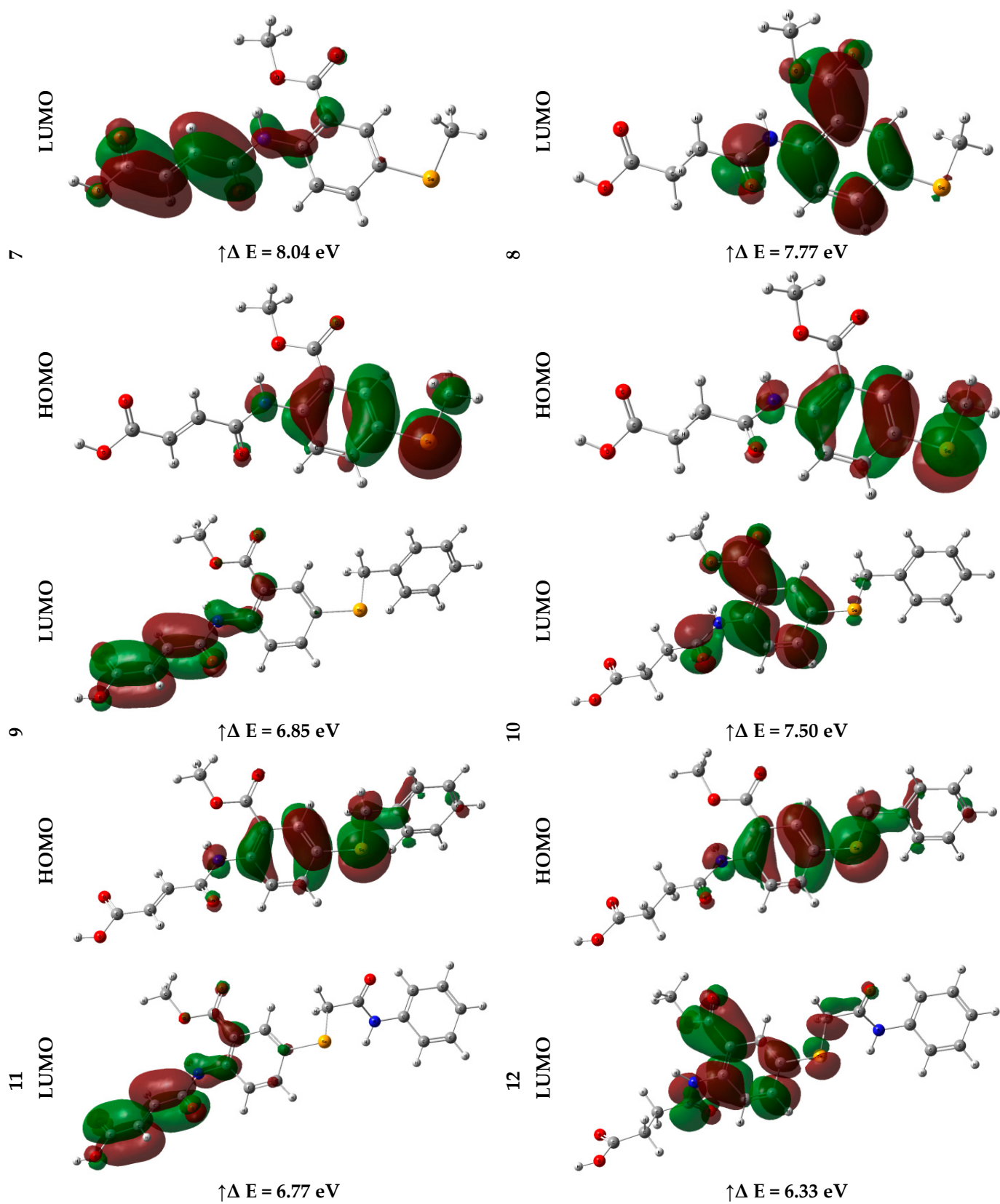


Figure 3. Cont.

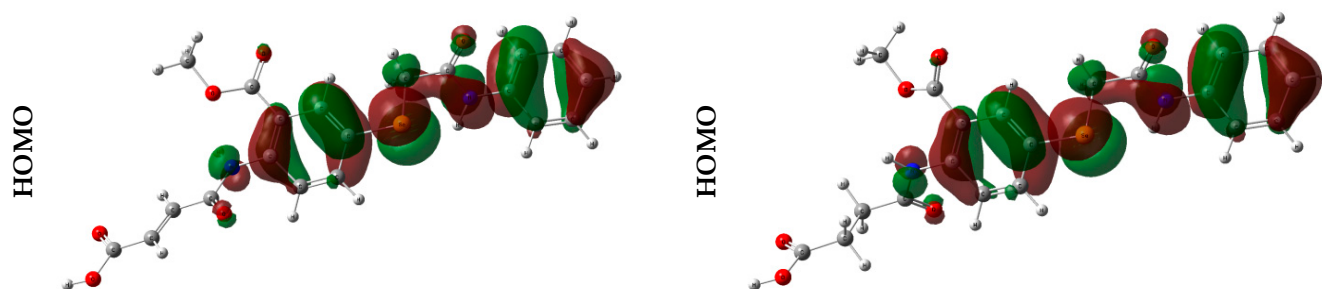


Figure 3. HOMO-LUMO of the optimized structures calculated using DFT/B3LYP.

Table 1. Calculated electronic parameters.

	E_{HOMO} (eV)	E_{LUMO} (eV)	ΔE (eV)	IP (eV)	EA (eV)	χ (eV)	CP (eV)	η (eV)	σ (eV ⁻¹)	ω (eV)	Nu (eV ⁻¹)
7	-8.94	-0.90	8.04	8.94	0.90	4.92	-4.92	4.02	0.12	3.01	0.33
8	-8.70	-0.93	7.77	8.70	0.93	4.82	-4.82	3.88	0.13	2.99	0.33
9	-8.58	-1.74	6.85	8.58	1.74	5.16	-5.16	3.42	0.15	3.89	0.26
10	-8.67	-1.17	7.50	8.67	1.17	4.92	-4.92	3.75	0.13	3.23	0.31
11	-8.56	-1.79	6.77	8.56	1.79	5.18	-5.18	3.39	0.15	3.96	0.25
12	-8.23	-1.90	6.33	8.23	1.90	5.06	-5.06	3.16	0.16	4.05	0.25

2.2.4. Global Reactivity

Potential data for predicting the relationship between the structure and biological properties include chemical reactivity, polarizability, kinetic stability, hardness–softness, and HOMO–LUMO energies. The HOMO (highest occupied molecular orbital) is the furthest orbital containing electrons and is responsible for donating them to other orbitals. The LUMO (lowest unoccupied molecular orbital) characterizes the electron acceptor for the innermost occupied orbital.

As a result, HOMO–LUMO orbitals influence whether a molecule is likely to be attacked by electrophiles or nucleophiles. Table 1 compares the values of E_{HOMO} and E_{LUMO} and shows that when E_{HOMO} is higher, electron transfer from the substrate to the target proteins is easier. On the other hand, a lower E_{LUMO} value indicates easier electron transfer between the substrate and target proteins. The likelihood of donating and accepting electrons increases in the following order: $12 > 11 > 9 > 10 > 8 > 7$.

The value of the energy gap (ΔE) between E_{LUMO} and E_{HOMO} provides insight into the reactivity levels of the molecules. A smaller ΔE value indicates that the molecule will more likely benefit from docking. As a result, the combined reactivity of the compounds can be ranked as follows: $12 > 11 > 9 > 10 > 8 > 7$.

Hardness and softness are essential in determining a molecule's position in the chemical reactivity ranking. The hard–soft–acid–base (HSAB) principle explains a molecule's tendency to bond with another. According to this principle, strong acids react well with strong bases, whereas weak acids prefer weak bases. Soft biological molecules include enzymes, proteins, and other biological macromolecules. As a result, biomolecules are more likely to interact with soft molecules than hard ones. Biological activity increases when softness increases and hardness decreases [41]. Therefore, the correct order for reactions to occur is $12 > 11 > 9 > 10 > 8 > 7$ (Table 1).

The stability of the investigated compounds was supported by their chemical potential (cp), which measures their potential energy. A lower chemical potential (cp) value indicates greater stability. As a result, the compounds can be ranked in terms of stability as follows: $12 > 11 > 9 > 10 > 8 > 7$ (Table 1).

2.2.5. Molecular Electrostatic Potential (MEP)

Proteins and ligands have partial charges that are critical in determining how rapidly a protein can bind to a substrate. Utilizing the molecular electrostatic potential (MEP) map is one way to comprehend ligands' 3-dimensional structural and topological features. In addition, the MEP test determines which component of the molecular geometry is more important: the effect of the nuclei or the electrons [42].

MEP diagram values are represented by a spectrum of colors, from blue to red and everything in between. The MEP's blue (positive) and red (negative) parts are related to nucleophilicity and electrophilicity, respectively. The red color represents parts of the surface that are negatively charged (i.e., those areas where accepting an electrophile is more favorable). The increase in the negative charge of a compound after an interaction with an electrophile indicates the attraction of the key sites contained within the complex.

The B3LYP/6-311 (d, p) basis set was used to produce the MEP shown in Figure 4. Negative areas (shown in red-orange) in the substrates under discussion were located mainly in the oxygen and Se moieties due to the availability of electrons. This means that electrophiles may easily target these areas for assault. The blue color represents more positive areas, mostly in the hydrogen and carbon moiety. In protein–substrate intermolecular interactions, they are mostly pointed toward the hydrogen and carbon moiety, which may operate as an H-bond donor (see Figure 4).

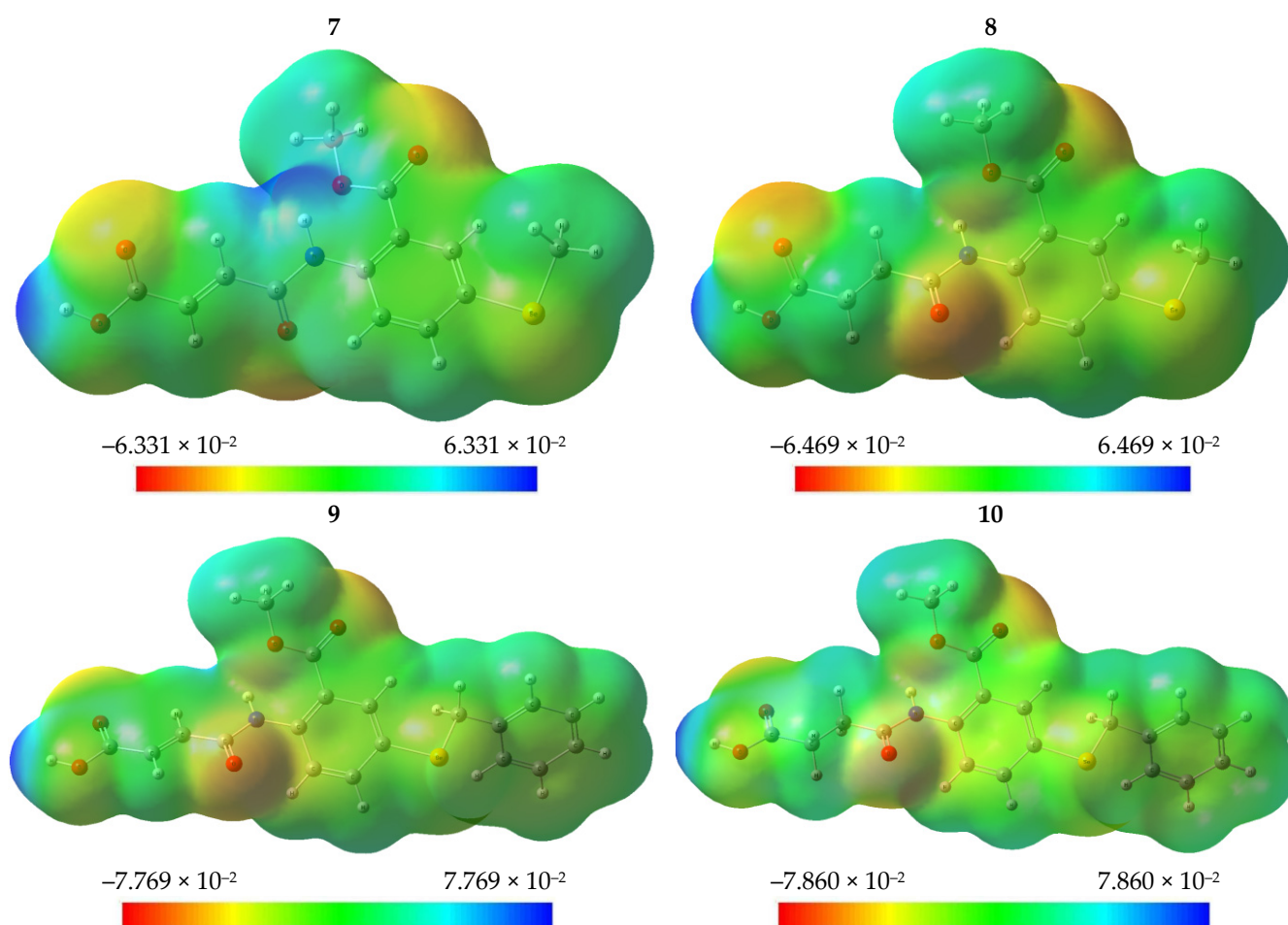


Figure 4. Cont.

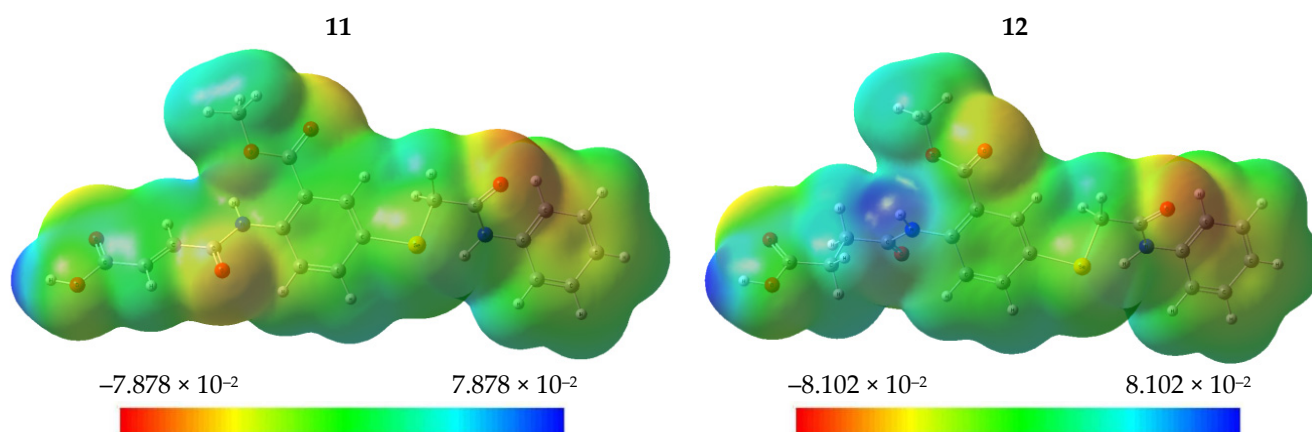


Figure 4. Optimized structures with atom labels using DFT/B3LYP.

2.2.6. Natural Charge Analysis

An atom's charge represents the molecule's physical features, including its electronic structure, vibrational spectrum, dipole moment, and polarizability. Natural bond orbital (NBO) calculations at the B3LYP/6-311G (d, p) level of theory were used to determine the atomic charges of the organic selenides; the results are shown in Figure S2 (see supporting information).

In the context of chemical reactivity, NBO analysis helps to clarify the role of electronegativity and charge transfer. From what we can tell from the NBO study, carbon atoms in organic selenides are both positively and negatively charged. Atoms bound to electron-withdrawing oxygen and nitrogen are positive in the NBO's supplementary file and Figure S2 (for more, see the Supporting Materials).

Additionally, the (C14, C7, C18), (C7, C14, C18), (C14, C7, C18), (C7, C14, C18), (C14, C7, C18), and (C7, C18, C14) atoms in the organic selenides 7–12, respectively, have the largest positive charges. In addition, the Se and all hydrogen atoms were positively charged. The fact that (O19), (O19), (O19), (O17), (O19), and (O19) atoms are electron-withdrawing means that the (H33), (H35), (H38), (H34), (H41), and (H43) hydrogen atoms in compounds 7–12 have the largest positive charges in contrast to other hydrogen atoms. All hydrogen atoms in 7–12 are positively charged. The most negatively charged carbon atoms in compounds 7–12 were (C6, C7, C15), (C12, C15, C17), (C12, C6, C17), (C12, C40, C43), (C12, C6, C17), and (C12, C17, C15) (Figure S2; see Supporting Information).

2.2.7. Natural Bond Orbital (NBO) Analysis

Realizing the properties of the electrical structure may be performed quickly using a method known as the natural bonding orbital (NBO) methodology. In addition, it is useful for analyzing charge transfer, delocalization, and conjugative interactions in molecules, as well as determining the interactions between donors and acceptors [43].

NBO analysis is an excellent method for investigating intra- and inter-molecular bonding because it offers a supporting modus operandi for analyzing charge transfer or hyperconjugative interactions. This makes it possible for the investigation to be carried out efficiently. The rehybridization, intramolecular charge delocalization, and electron density computations inside the molecules were carried out using NBO 5.0 software using the Gaussian 9 W program. Quantitative analysis of bonding and anti-bonding interactions caused by second-order perturbation was performed using the NBO method [44,45]. This method expresses perturbation energies as $E(2), E(2) = \Delta E_{ij} = q_i(F_{i,j})^2 / E_j - E_i$, where E_i and E_j are diagonal elements, q_i is donor orbital occupancy, and $F_{i,j}$ is an NBO off-diagonal matrix element (for more information, see the NBO Supplementary Information file).

The interactions that are estimated to be the most effective between the Lewis-type occupied NBO orbital (bonding) and non-Lewis unoccupied NBO orbital (anti-bonding) are provided in NBO Supplementary Information file for all the compounds. These interactions

are presented in order from the most efficient to least efficient. The nearby examination of the different donors and acceptors indicates that there are just two sorts of donors, σ and π , and two kinds of acceptors, σ^* and π^* . The observation of perturbation energy E (2) for different transitions shows the chances in the following transitions were highly probable for molecule 7: C1–C3 \rightarrow C2–C4 (121.26 kJ/mol, $\pi^* \rightarrow \pi^*$), N13 \rightarrow C14–O16 (5075 kJ/mol, LP $\rightarrow \pi^*$), C14–O16 \rightarrow C15–C17 (47.23 kJ/mol, $\pi^* \rightarrow \pi^*$), and O19 \rightarrow C18–O20 (40.52 kJ/mol, LP $\rightarrow \pi^*$); for molecule 8: C1–C3 \rightarrow C2–C4 (129.94 kJ/mol, $\pi^* \rightarrow \pi^*$), N13 \rightarrow C14–O16 (50.70 kJ/mol, LP $\rightarrow \pi^*$), O8 \rightarrow C7–O9 (38.54 kJ/mol, LP $\rightarrow \pi^*$), and O19 \rightarrow C18–O20 (37.54 kJ/mol, LP $\rightarrow \pi^*$); for molecule 9: C1–C3 \rightarrow C2–C4 (119.88 kJ/mol, $\pi^* \rightarrow \pi^*$), N13–C14–O16 (50.66 kJ/mol, LP $\rightarrow \pi^*$), C14–O16 \rightarrow C15–C17 (47.13 kJ/mol, $\pi^* \rightarrow \pi^*$), and O19 \rightarrow C18–O20 (40.53 kJ/mol, LP $\rightarrow \pi^*$); for molecule 10: O18 \rightarrow C16 (6.05 kJ/mol, $\sigma \rightarrow \sigma^*$), O15 \rightarrow C14 (5.85 kJ/mol, $\sigma \rightarrow \sigma^*$), O9 \rightarrow C7 (5.28 kJ/mol, $\sigma \rightarrow \sigma^*$), and C19 \rightarrow C21 (2.19 kJ/mol, $\sigma \rightarrow \sigma^*$); for molecule 11: O22 \rightarrow C22 (9.61 kJ/mol, $\sigma \rightarrow \sigma^*$), O20 \rightarrow C18 (5.57 kJ/mol, $\sigma \rightarrow \sigma^*$), O16 \rightarrow C14 (5.53 kJ/mol, $\sigma \rightarrow \sigma^*$), and O9 \rightarrow C7 (5.25 kJ/mol, $\sigma \rightarrow \sigma^*$); and for molecule 12: C1–C3 \rightarrow C2–C4 (150.66 kJ/mol, $\pi^* \rightarrow \pi^*$), C5–C6 \rightarrow C2–C4 (130.87 kJ/mol, $\pi^* \rightarrow \pi^*$), N13 \rightarrow C14–O1 (48.43 kJ/mol, LP $\rightarrow \pi^*$), and N23 \rightarrow C21–O2 (42.73 kJ/mol, LP $\rightarrow \pi^*$) (see NBO Supplementary Information file).

The NBO analysis for Lewis and non-Lewis orbitals is also included in Tables S4–S6 (see Supplementary Material) for the organic selenides 7–12. These tables cover the range of organic selenides from 7–12. According to the findings, all core and valence Lewis orbitals had much greater occupancy than the threshold occupancy values, indicating that the optimized Lewis structures were stable. In addition, a detailed breakdown of Lewis and non-Lewis's occupancies into the core, valence, and Rydberg shell contribution are shown in the NBO Supplementary Information file, which indicates the quality of the natural Lewis structure description in terms of the percentage of the overall electron density. Therefore, more than 97–90% of the Lewis core and valence shells and around 1.5–3.5% of the contribution came from the non-Lewis shells for each of the three compounds. Considering this knowledge, it was hypothesized that the Lewis orbitals predominated the optimized shape (see the NBO Supplemental Information file for further details).

2.3. Drug Likeness Screening

Lipinski's rule of five outlines the characteristics of medicine that must be present to be considered a candidate for drug design [46,47]. For a substrate to be considered drug-like, it must fulfill the following criteria: it must have a molecular weight (M.wt) of 500, the number of H-bond acceptors (NHBA) must be 10, the number of H-bond donors (NHBD) must be 5, and its lipophilicity must be stated as $\log P \leq 5$ [48]. Only then can the substrate be considered drug-like. All the compounds in the issue satisfy the criteria outlined in the Lipinski rule of five, which can be found in Table S1. This offers compelling evidence that the compounds in question are acceptable for use as pharmaceuticals.

Martin [49] developed the Abbot bioavailability score, sometimes known as the ABS. This score works on the premise that at least 10% of substances are anticipated to be bioavailable in rats. The ABS for compounds are computed to be 0.55 if the Lipinski rule of five is followed perfectly; otherwise, it is calculated to be 0.17. If the rule of five is followed precisely, the ABS for compounds is 0.55. These compounds have met the requirement for drug similarity due to their ABS value of 0.56, which indicates that these compounds are comparable with drugs.

There is a connection between the requirements for drug-likeness and water solubility (assessed in logs) and gastrointestinal absorption permeability (measured in G.I.). Additionally, they are used to evaluate the preliminary stages of oral bioavailability. The $\log K_p$ value for skin permeability is often found to fall somewhere in the range of 8.0 to 1.0. The $\log S$ values for the studied compounds range from 2.58 to 4.19, which indicates that the compounds in question have a low water solubility [50] and excellent absorption in the gut (except 7 and 9) [49,51–53]. All the medications that were shown to have considerable absorption levels in the gastrointestinal system were shown to have positive ADME out-

comes. Nothing in this list can pass the blood–brain barrier (BBB) or serve as a substrate for the P-glycoprotein (Pgp) enzyme.

In addition, an analysis was conducted to determine how easily the chemicals under examination might be synthesized. It is produced from 1024 separate fragment contributions, each constrained by size and complexity [54]. Its score runs from 1 (extremely easy) to 10 (very tough) and may be anywhere in between. The synthetic accessibility, which varied from 2.756 to 3.36, suggested that the compounds in question were easy to synthesize and predicted that they would be accessible with excellent yield. These projections were in keeping with the experiment's outcomes, demonstrating that the compounds were indeed available in good yield.

In addition, the bioavailability radar can swiftly assess whether a chemical acts like a drug by analyzing parameters such as the chemical's saturation, lipophilicity, polarity, size, solubility, and flexibility. This allows the bioavailability radar to evaluate whether a chemical behaves like a medication. Figure 5 provides a graphical depiction of these physicochemical characteristics for the compounds studied. The pink zone within the hexagon represents the optimal range for each characteristic, and this range varies depending on the property.

The SwissADME online web server was responsible for developing the brain or intestine estimated permeation prediction model, sometimes called BOILED–Egg [55]. This model was used to predict the quantity of absorption in the brain and the gastrointestinal system for nine different steroids. Nine steroids were supplied in Figure 6. According to the findings, taking in any material via the mouth is possible and will favor absorption in the digestive system. Consequently, no substance can get through the BBB, which protects the population from any potentially negative effects that may be had on the CNS. Furthermore, because none of the compounds are present, there is no danger to those sensitive to P-glycoprotein. Consequently, we anticipate very little to no resistance.

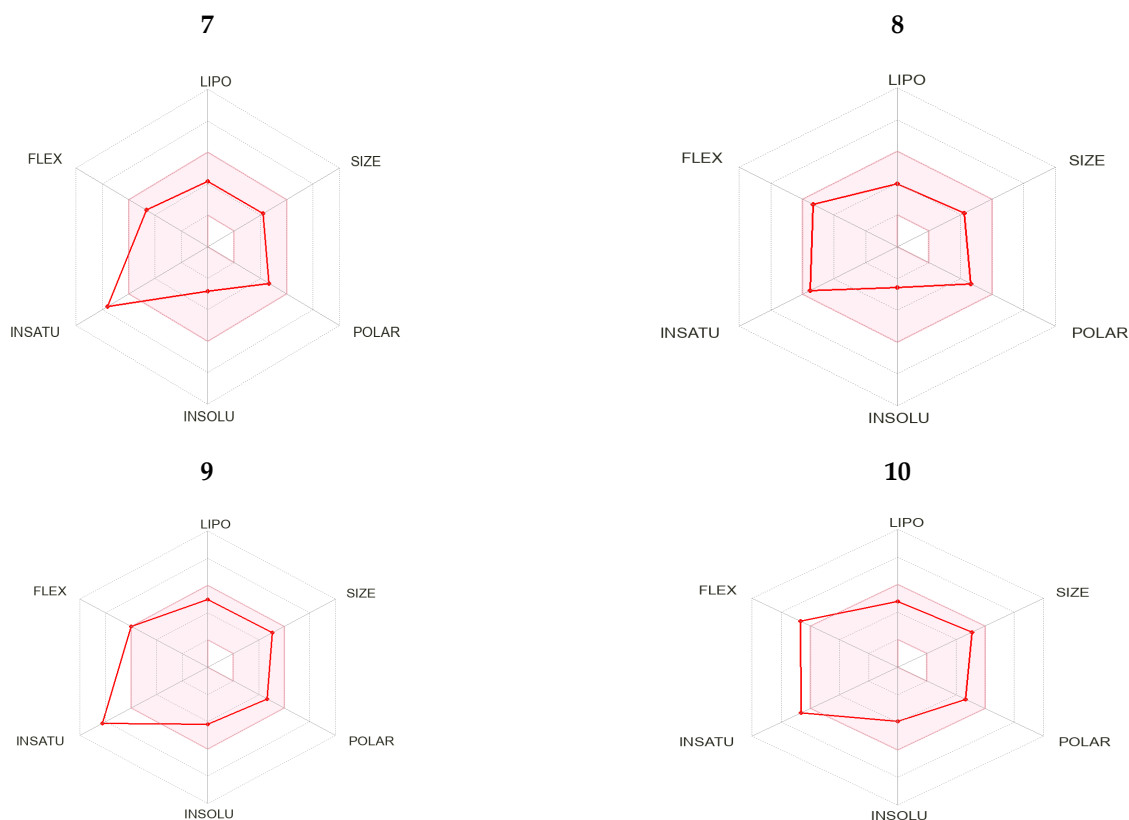


Figure 5. Cont.

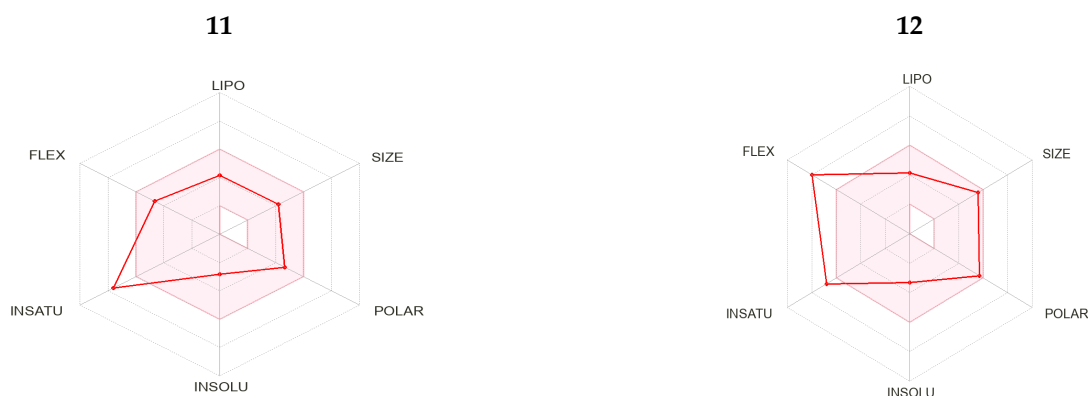


Figure 5. The colored zone is the suitable physicochemical space for oral bioavailability; LIPO (Lipophilicity), SIZE: (Mwt.), POLAR (Polarity), INSOLU (Insolubility), INSATU (Instauration), FLEX (Flexibility).

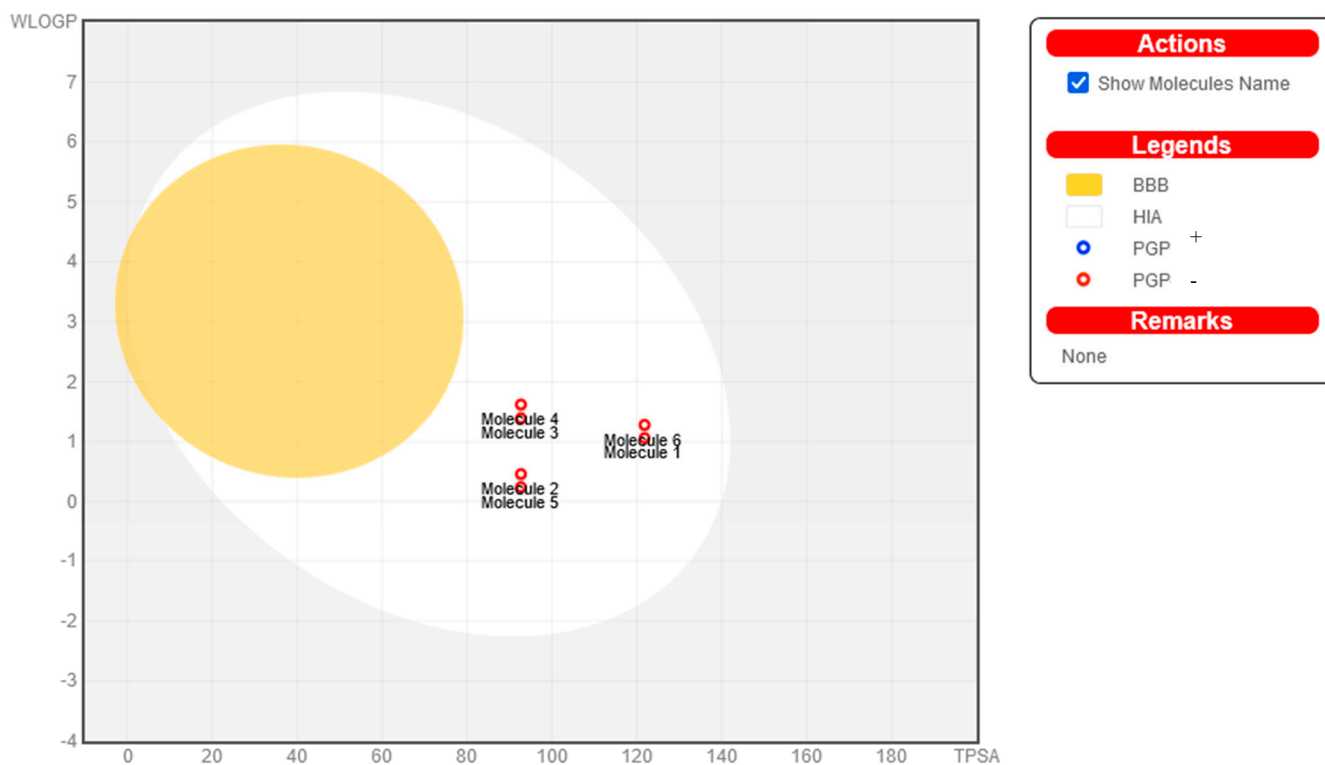


Figure 6. The bioavailability radars of the newly obtained derivatives. Molecule 1 (7), molecule 2 (8), molecule 3 (9), molecule 4 (10), molecule 5 (11), and molecule 6 (12).

2.4. Pharmacokinetic Properties

It is possible to obtain an approximation of a drug candidate's pharmacokinetic profile using the ADMET profile. In the early stages of developing a new medicine, performing an ADMET analysis may be very beneficial in enabling a significant reduction in the number of failed clinical trials [56]. The lead compounds that were under investigation were subjected to the ADMET method. Aqueous solubility, gastrointestinal (GI) absorption, skin permeability, and Caco2 permeability are the important absorption characteristics studied in the pharmaceutical industry [57]. Compound 10 had the highest significant absorption percentage, 50.07 percent, followed by Compound 9 at 49.29 percent and Compound 12 at 46.38 percent; these compounds exhibited good absorbance rates (Table S2). A value for skin permeability that is more than -2.5 cm/h is considered poor, yet every therapeutic agent displayed exceptional skin permeability. Caco2 permeability was very low (less than

0.9 cm/s) in every possible therapy option. Another essential aspect of the ADMET study was predicting whether a P-glycoprotein may serve as a non-substrate candidate. It was found that any substance might serve as a substrate for P-glycoprotein (see Table S2 for further information).

To obtain a better understanding of how medications are dispersed throughout the body, researchers [58] have investigated the permeability of the membranes that make up the VDSS, the CNS, and the BBB. The decline in log VDss from -0.99 to -1.20 was at the lower end of the scale. As far as the permeability of the BBB membrane is concerned, log BB values ranging from -0.2 to -0.9 indicated that the drug molecules could be able to overcome the barrier. However, it was impossible for the central nervous system (CNS) to penetrate log PS levels that ranged from -2.8 to 3.3 . It was hypothesized that because of this, none of the potential medications would be able to reach the central nervous system or pass through the barrier that separates the blood from the brain (Table S2).

The CYP450 enzyme is critical to the process of drug metabolism that occurs in the liver [58]. There was no evidence that any of the pharmaceutical substances altered or inhibited the CYP2D6 and CYP3A4 enzymes, as shown by the findings of the metabolism tests. In addition, the pharmacological compounds did not affect the enzymes CYP2D6, CYP2A4, CYP2C9, or CYP2C19 by acting as inhibitors of those enzymes. Therefore, it is vital to consider both hepatic and renal clearance to measure total drug clearance accurately. In addition, the elimination rate of the medicine may be utilized in conjunction with the total clearance to describe the drug's concentration in the body [59]. Excretion rates of the possible candidates for new medications ranged from 1.82 to 2.21 mL/min/kg, as predicted by the results (Table S2), which may be seen in the accompanying table.

Cytotoxicity is essential to consider while creating new medications [60] related to the pharmaceutical industry. Except for compound **10**, no other OSe compound exhibited any allergy signals for the skin or any hepatotoxic effects (Table S2). hERG inhibition, in both its I and II forms, is an essential part of the process of toxicity evaluation and is linked to cardiotoxicity. No chemical in the test showed any signs of an inhibitory impact on hERG I or hERG II inhibitors. In addition, none of the possible medications showed any sign of toxicity when tested on either AMES or tetrahymena pyriformis. The toxicity analysis server predicted the maximum tolerated dosage range, the lowest observed adverse effect level (LOAEL), and the LD50 of the pharmaceutical candidates. The results that it generated are shown in Table S2. Based on these results, the present study concluded that these bioactive drug candidates might be used as potential treatments for inhibiting the proteases involved in COVID-19.

2.5. Molecular Docking

When attempting to determine the pharmacological efficiency, researchers often evaluate the degree to which ligands are sensitive when interacting with their primary targets (proteins) [36]. As a result, a technique was employed throughout this study to examine the interaction between the chemicals of interest and the protein that was the primary focus of the investigation.

The molecular docking approach is now being utilized to produce predictions regarding the biological effectiveness of the compounds. This method establishes not only the ideal orientation of the ligand when it binds to the side pocket on the targeted protein but also finds the ligand's optimal orientation. It is now possible to make these kinds of predictions using a method known as molecular docking.

The main protease (Mpro) of the SARS-CoV-2 virus is a cysteine enzyme critical for viral replication and transcription, thus indicating a potential target for antiviral therapy. In the course of this research, the compounds that were developed were docked to the SARS-CoV-2 Mpro complex (PDB: 7BFB) so that it could be determined whether or not they were suitable candidates for antiviral therapy. Because of the virtual compound screening and scoring functions utilized in the study, molecular docking studies enabled the prediction of the most remarkable binding affinities [34,61]. In addition, this approach

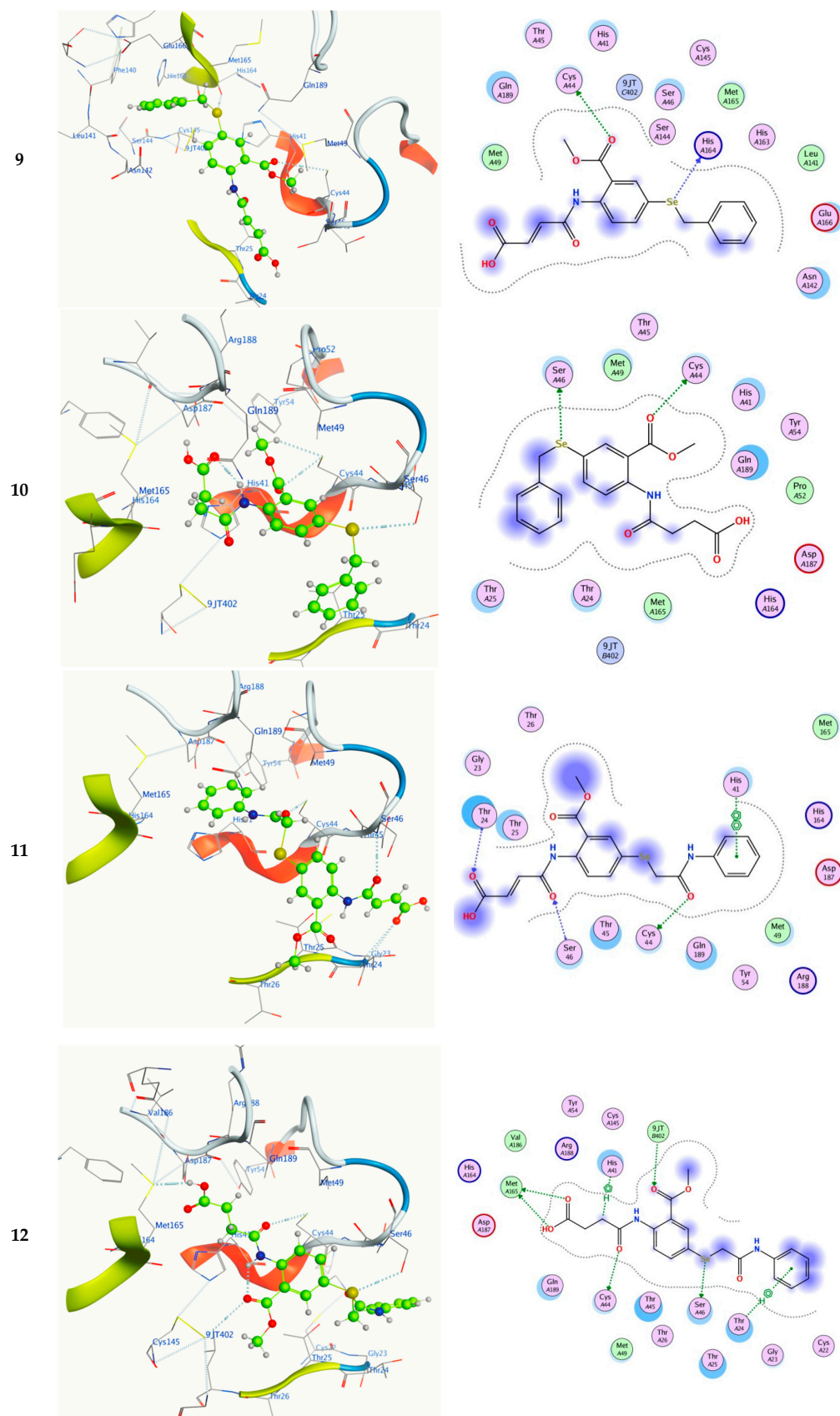


Figure 7. The 3D structure of the SARS-CoV-2 M^{Pro} complex (PDB: 7BFB) of the novel coronavirus (COVID-19) (a); active site pocket in which molecular docking occurred (b); and 3D and 2D interactions of the title compounds inside the active site of the target receptor (c).

Table 2. Molecular docking data; interaction type, and distance between ligand and receptor of the title compounds.

7bfb	Ligand	Receptor	Interaction	Distance	E (kcal/mol)	S (kcal/mol)	RMSD	Ki (μM)
7	O16	CYS 44	H-donor	3.16	−1.00	−6.97	1.17	7.85
	O19	MET 165	H-donor	3.42	−3.20			
	O9	9JT 402	H-acceptor	3.93	−0.70			
8	C10	9JT 402	H-donor	4.04	−0.60	−6.84	1.56	9.77
	O16	CYS 44	H-donor	3.37	−0.90			
	O19	MET 165	H-donor	3.05	−3.80			
	O20	MET 165	H-donor	3.31	−0.20			
	O9	9JT 402	H-acceptor	3.46	−0.70			
9	O9	CYS 44	H-donor	3.95	−0.90	−7.23	1.43	5.09
	SE11	HIS 164	H-donor	3.37	−0.90			
10	O9	CYS 44	H-donor	3.17	−0.90	−7.62	1.49	2.65
	SE11	SER 46	H-donor	3.44	−1.90			
11	O22	CYS 44	H-donor	3.31	−0.80	−8.20	1.36	0.99
	O16	SER 46	H-acceptor	2.91	−1.10			
	O20	THR 24	H-acceptor	3.25	−0.70			
	6-ring	HIS 41	pi-pi	3.99	−0.54			
12	SE11	SER 46	H-donor	3.25	−0.70	−8.49	1.08	0.61
	O16	CYS 44	H-donor	3.33	−1.50			
	O19	MET 165	H-donor	3.16	−4.10			
	O20	MET 165	H-donor	3.30	−0.20			
	O9	9JT 402	H-acceptor	3.65	−0.90			
	C15	HIS 41	H-pi	3.73	−1.00			
	6-ring	THR 24	pi-H	4.10	−0.60			

As is shown in Table 2 and Figure 7c, the docking scores (S) for the subject substrates are significantly on the negative side. They connect to the 7BFB pocket in several different ways, including via hydrogen bonds and interactions that are hydrophobic. This suggests that the docked substrates are engaging in a robust interaction with the active region of the receptor. According to Table 2, the compounds tested have low RMSD values and high docking scores (regarding S and Kcal/mol) regarding the 7BFB. These values varied from −8.49 kcal/mol and 1.08 for compound 12 to −6.84 kcal/mol and 1.56 for compound 8. As a consequence, compound 12 seems to be the most energetic candidate because it has a high docking score (−8.49 Kcal/mol) and a low RMSD value (1.08). The following is a list of the levels of inhibitory activity in the order that they were reached: 12 > 11 > 10 > 9 > 7 > 8, Table 2. The docking results show that the compounds with the highest activity level were compounds 12, 11, and 10.

Compound 12 creates four hydrogen bond donors: SE11, O16, O19, and O20 with SER46, CYS44, MET165, and MET165, with distances of 3.25, 3.33, 3.16, and 3.30 angstroms, respectively. In addition to one hydrogen bond acceptor, one H-pi and one pi-H interactions between O9 with 9JT402, C15 with HIS4, and 6-ring with THR24, with distances of 3.65, 3.73, and 4.10 angstroms, respectively, occur (Table 2 and Figure 7c). compound 11 creates one hydrogen bond donor: between O22 with CYS44, with a distance of 3.31 angstroms. Two hydrogen bond acceptors and one pi-pi interaction between O16 with SER46, O20 with

THR24, and 6-ring with HIS41, with distances of 2.91, 3.25, and 3.99 angstroms, respectively, occur (Table 2 and Figure 7c). Compound 10 creates two hydrogen bond donors: between O9 and SE11 with CYS44 and SER46, with distances of 3.17, and 3.44 angstroms (Table 2 and Figure 7c).

The inhibition constant, sometimes referred to as the K_i value, is a critical component that is taken into consideration when deciding whether or not a molecule has the potential to be a hit, lead, or therapeutic candidate [62]. For a molecule to be considered a hit or a lead chemical, the K_i value of the molecule must fall within the micromolar (μM) range. This is because, in most cases, a low K_i number indicates a high potency. The 7BFB domain K_i values of the discovered compounds varied from 0.61 μM (in the case of compound 12) and 0.99 μM (in the case of compound 11) to 9.77 (in the case of compound 8), which shows that every single one of them has the potential to be a hit or a lead. Accordingly, therapeutic applications are a viable option for the compounds produced and shown to have the low K_i values (Table 2).

In addition, the titled compounds were used as ligands (substrates) for investigation of their binding ability towards the SARS-CoV-2 protease (PDB ID: 6LU7), and the results are discussed in the Supplementary Information file (SI.3).

2.6. Molecular Dynamics (MD) Simulations

To evaluate the exact behavior of the most active compound (12) within the M^{Pro} binding pocket of SARS-CoV-2 (PDB ID: 7BFB) compared with its co-crystallized inhibitor (Co), the MD simulations were run for 200 ns.

2.6.1. RMSD Analyses

It is a very crucial tool to describe the degree of deviation relative to the initial position of each studied complex. This evaluates the total system stability during the simulation time.

The maximum value for the RMSD of the 12–7BFB complex (2.2 Å) was comparable with that of the Co–7BFB complex (2 Å), Figure 8. This indicates the very high stability of the 12–protein complex, with similar behavior to that of the Co as well.

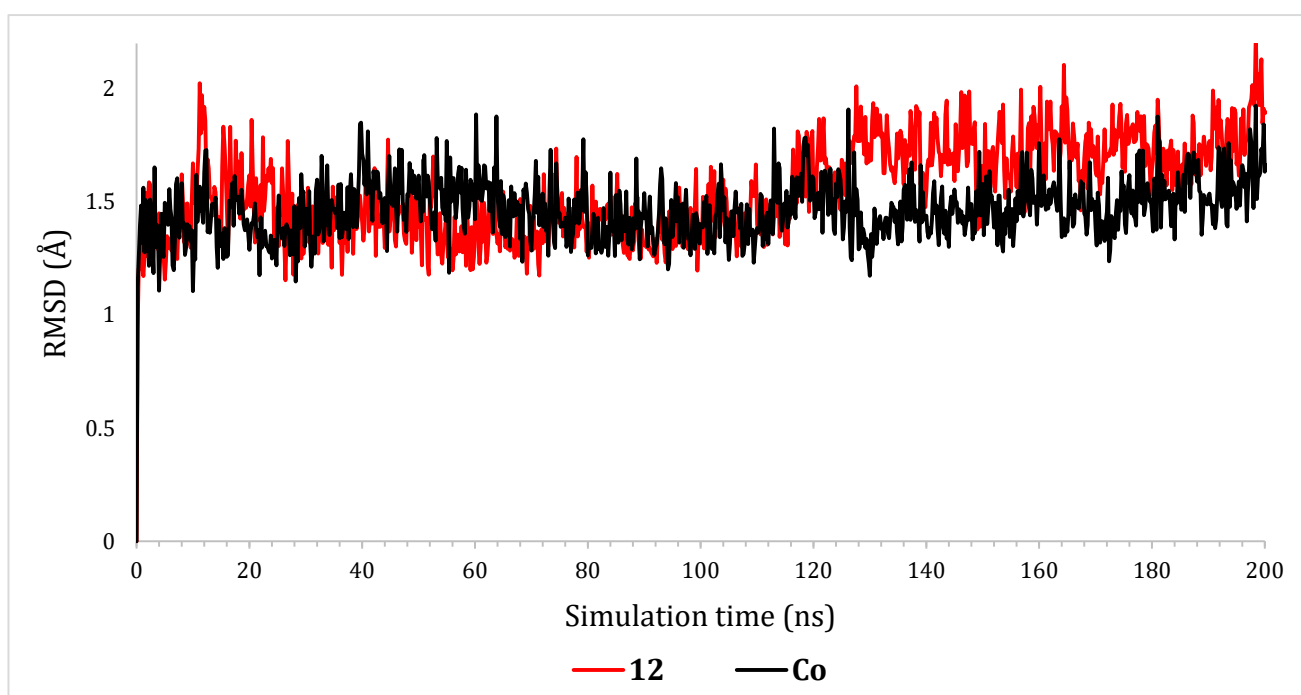


Figure 8. The RMSD of complexes (12 and Co) for the SARS-CoV-2 M^{Pro} binding site (PDB ID: 7BFB) as a function of simulation time (200 ns).

On the other hand, the ligand RMSD for the 12–7BFB complex throughout the 200 ns of the simulation time was <10 Å. However, that of the Co–7BFB reached 11.5 Å, Figure 9. This indicates the superior behavior of compound 12 within the binding pocket of SARS-CoV-2 M^{Pro} compared with that of the Co.

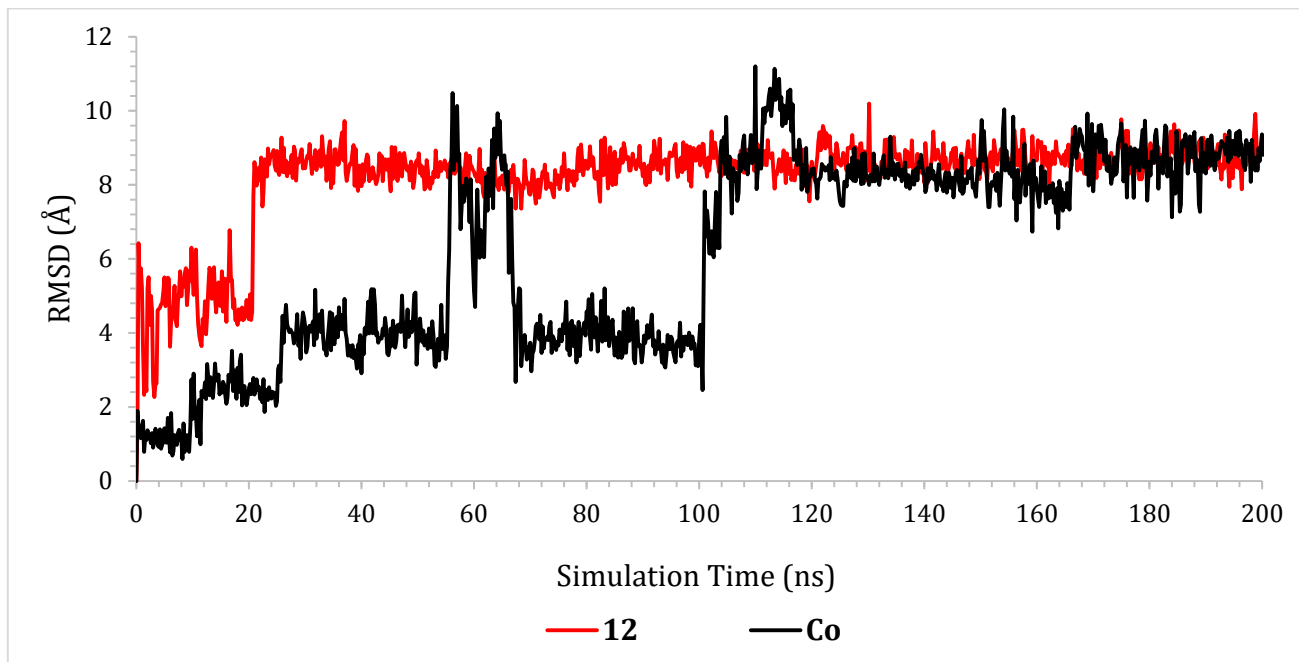


Figure 9. The RMSD of ligands (12 and Co) for the SARS-CoV-2 M^{Pro} binding site (PDB ID: 7BFB) as a function of simulation time (200 ns).

Compound 12 showed moderate fluctuations from the start until 20 ns where it reached around 9 Å and stayed at the same level with minor fluctuations until 200 ns. However, the reference Co showed large fluctuations in the first 120 ns, especially from (55–70) and (100–120) ns. Then, it was stabilized at around 9 Å until the end of the simulation time.

Based on the above, we could conclude that the behavior of compound 12 within the binding site of SARS-CoV-2 M^{Pro} was superior to its reference Co, indicating a very promising inhibition for the M^{Pro} of SARS-CoV-2.

2.6.2. Histogram and Heat Map Analyses

To describe the types and percentages of the interactions between the receptor pocket amino acids and the examined compounds, the histogram charts were analyzed accordingly in Figure 10.

The histogram of 12–7BFB showed that Gln189, Met49, and Tyr54 were the most crucial amino acids in the interactions with 115, 80, and 65%, respectively. The types of interactions were hydrogen bonds, ionic bonds, and water bridges for Gln189, hydrophobic interactions for Met49, and water bridges for Tyr54, Figure 10A.

However, the Co–7BFB histogram showed that His41, Gln189, and Arg188 were the most important amino acids in the interactions with 48, 40, and 35%, respectively. Moreover, the types of interactions were described as hydrophobic interactions and water bridges for His41 and hydrogen bonds and water bridges for both the Gln189 and Arg188 amino acids, Figure 10B.

Therefore, the Gln189 amino acid was found to be the most important for the binding to the interacting inhibitor within the binding pocket of SARS-CoV-2 M^{Pro}.

The heat maps for the studied two complexes (12–7BFB and Co–7BFB) are described in Figure 11. This represents the interactions of the most important amino acids of SARS-CoV-2 M^{Pro} relative to the simulation time (200 ns).

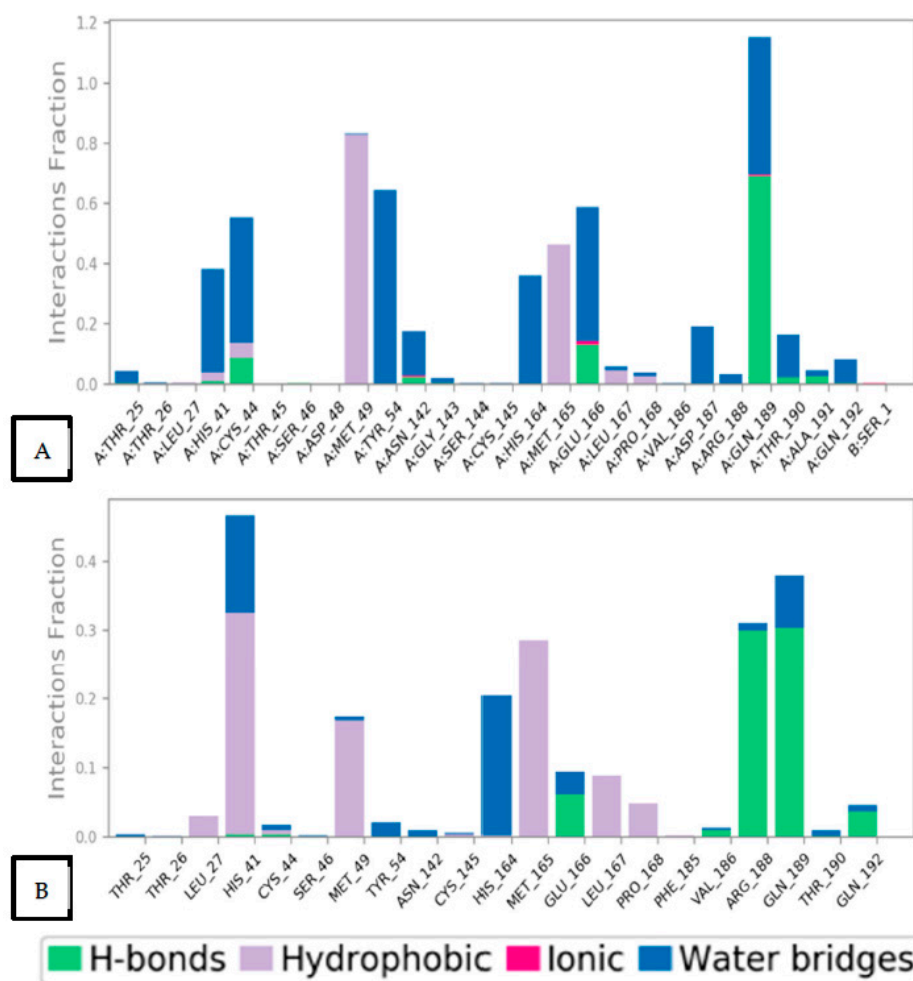


Figure 10. Histogram describing the binding interactions between the SARS-CoV-2 M^{Pro} protein (PDB ID: 7BFB) and its ligand during the simulation time of 200 ns for (A) 12 and (B) Co.

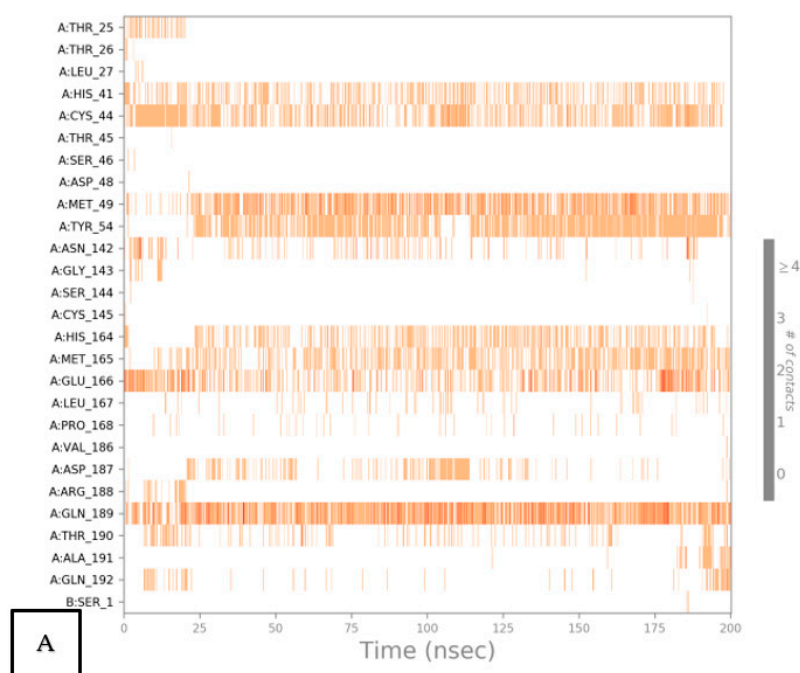


Figure 11. Cont.

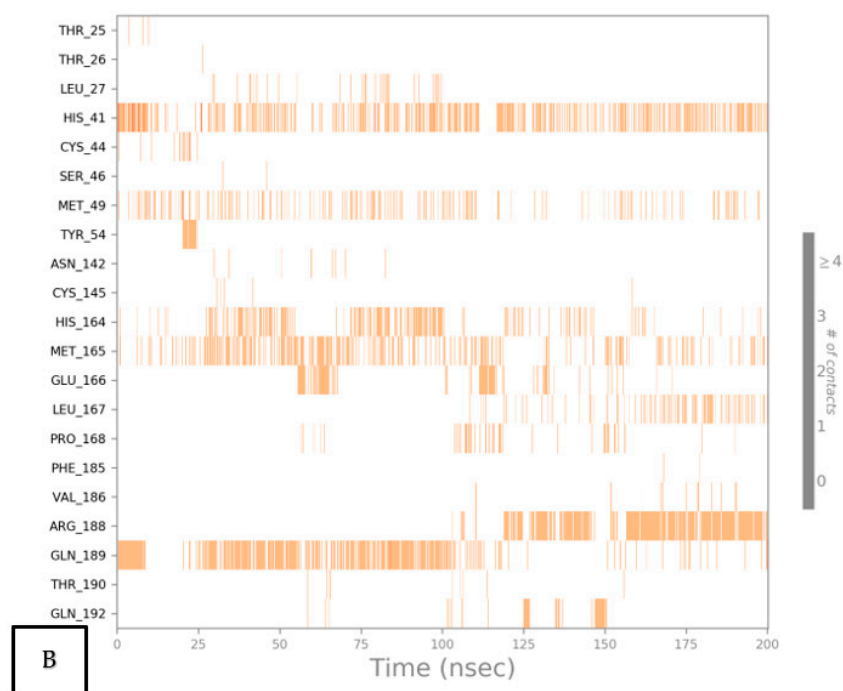


Figure 11. Heat map showing the total number of SARS-CoV-2 M^{Pro} protein (PDB ID: 7BFB)–ligand interactions all over the simulation time of 200 ns for (A) **12** and (B) Co.

The heat map of the **12**–7BFB complex showed that Gln189 interactions increased gradually from the start until 20 ns and stayed until the end of the simulation time. Met49 interactions were unnoticed until 25 ns, where they remained obvious to the end of the simulation time. However, Tyr54 interactions started at 25 ns until the end of the simulation time and only disappeared from 100 to 117 ns, Figure 11A.

Furthermore, the heat map of the reference Co–7BFB complex clarified that His41 interactions were more prominent at the start and the end of the simulation time. Gln189 interactions nearly disappeared after the first 100 ns of the simulation time. Moreover, Arg188 interactions started from 100 ns and became more intense after 150 ns until the end of the simulation time, Figure 11B.

2.7. Prime MM-GBSA Calculations and MD Trajectory Analysis

The lipophilic, covalent, hydrogen bonding, coulomb, generalized Born electrostatic solvation, and Van der Waals energies were calculated (Table 3) using the thermal_mmgsba.py python script of Schrodinger [63,64].

Table 3. Prime MM-GBSA energies for complexes (**12** and Co–7BFB) of the SARS-CoV-2 M^{Pro} receptor.

Complex	ΔG Binding	Coulomb	Covalent	H-bond	Lipo	Bind Packing	Solv_GB	VdW	St. Dev.
12	−59.07	13.64	−0.60	−1.00	−16.09	−1.47	−2.55	−50.99	4.91
Co	−47.53	−5.46	1.70	−0.45	−15.27	−1.27	11.56	−38.34	4.10

Covalent: Covalent binding energy; Coulomb: Coulomb energy; Lipo: Lipophilic energy; H-bond: Hydrogen bonding energy; Solv_GB: Generalized Born electrostatic solvation energy; VdW: Van der Waals energy; and St. Dev.: Standard deviation.

According to Table 3, we can observe that compound **12** achieved a greatly superior ΔG binding energy (−59.07 kcal/mol) than the reference Co (−47.53 kcal/mol). This shows a very promising affinity and an intrinsic anti-SARS-CoV-2 activity for compound **12**. Moreover, the covalent, hydrogen bonding, lipophilic, bind packing, generalized Born

electrostatic solvation, and Van der Waals energies of compound **12** were observed to be better than those of the reference Co.

3. Experimental

3.1. Material and Methods

Melting points were recorded in degrees centigrade on a Gallenkamp instrument using the standard open capillary method. The IR spectra were recorded on a FTIR 5000 Mattson spectrophotometer for reagents 2–6 and products 7–12 on KBr pallets between 4000 and 400 cm^{-1} and 4000 and 640 cm^{-1} , respectively. The ^1H and ^{13}C -NMR spectra were recorded in $\text{DMSO}-d_6$ on a Varian 400 and 500 Spectrophotometer (^1H : 400 and 500 MHz, ^{13}C : 101 and 125 MHz) at 295 K. The chemical shifts (δ) are given in parts per million (ppm) downfield relative to tetramethyl silane (TMS). Mass spectra were recorded on a Bruker micrOTOFQ II APPI mass spectrometer. Compounds 2–6 were obtained according to our literature reports [32,65], and the new compounds 7–12 were fully characterized (see detailed experimental procedures in the Supplementary Information).

3.2. Synthesis and Characterization

The synthesis of OSe maleanilic **7**, **9**, and **11** and succinilic **8**, **10**, and **12** derivatives: maleic or succinic anhydride (1.3 mmol) was added to OSe amine (1.0 mmol) in methylbenzene (3.0 mL). The solution was stirred for 8 hrs. Then, the formed precipitate was filtered and washed with warm methylbenzene and water. The acids were obtained in enough purity and no further purifications were needed.

3.2.1. Synthesis of (Z)-4-((2-(Methoxycarbonyl)-4-(Methylselanyl)Phenyl)Amino)-4-Oxobut-2-Enoic Acid (**7**)

Compound **7** was obtained from methyl 2-amino-5-(methylselanyl)benzoate (**4**) (1.0 mmol, 245 mg) and maleic anhydride (1.3 mmol, 127 mg). The reaction was followed by TLC (CH_2Cl_2 /methanol 5%; $R_f = 0.30$), isolated as a yellow solid with 78% yield (269 mg), and its m.p. = 155–156 °C. IR (FT-IR, cm^{-1}): 3220 (N-H), 3100 (broad O-H, carboxylic acid), 3050 ($\text{C}_{\text{Ar}}\text{-H}$), 2963 ($\text{C}_{\text{aliph}}\text{-H}$), 2881 ($\text{C}_{\text{aliph}}\text{-H}$), 1705 (C=O, ester), 1625 (C=O, carboxylic), 1595 (C=O, amide), 1574 (C=C), 1425 (C=C), 1301 ($\text{C}_{\text{Ar}}\text{-N}$), 1106 (C-O), 954, 842, 816 (1,2,4-trisubstituted benzene); ^1H NMR (500 MHz, $\text{DMSO}-d_6$) δ 13.01 (s, 1 H, COOH), 10.69 (s, 1 H, NH), 8.10 (d, $J = 8.6$ Hz, 1 H, Ar-H), 7.88 (d, $J = 2.2$ Hz, 1 H, Ar-H), 7.68 (dd, $J = 8.6, 2.2$ Hz, 1 H, Ar-H), 6.54 (d, $J = 12.4$ Hz, 1 H, =CH), 6.35 (d, $J = 12.4$ Hz, 1 H, CH=), 3.83 (s, 3 H, OCH_3), 2.37 (s, 3 H, SeCH_3); ^{13}C NMR (126 MHz, $\text{DMSO}-d_6$) δ 166.68, 166.50, 163.28, 136.60, 135.01, 132.02, 131.20, 130.05, 126.24, 122.44, 119.55, 52.46, 7.00. MS (ESI): $m/z = \text{found } 366.1 [\text{M}^+ + \text{Na}]$; calcd. 366.0 [$\text{M}^+ + \text{Na}$]. Anal. Calcd. for $\text{C}_{13}\text{H}_{13}\text{NO}_5\text{Se}$ (343.00) C, 45.63; H, 3.83; N, 4.09. Found C, 45.66; H, 3.82; N, 4.07.

3.2.2. Synthesis of 4-((2-(Methoxycarbonyl)-4-(Methylselanyl)Phenyl)Amino)-4-Oxobut-2-Enoic Acid (**8**)

Compound **8** was obtained from methyl 2-amino-5-(methylselanyl)benzoate (**4**) (1.0 mmol, 245 mg) and succinic anhydride (1.3 mmol, 130 mg). The reaction was followed by TLC (CH_2Cl_2 /methanol 5%; $R_f = 0.33$) and isolated as a yellow solid with 91% yield (313 mg) and its m.p. = 136–137 °C. IR (FT-IR, cm^{-1}): 3313 (NH), 3200 (broad O-H, carboxylic acid), 3027 ($\text{C}_{\text{Ar}}\text{-H}$), 2912, 2849 ($\text{C}_{\text{aliph}}\text{-H}$), 1685 (C=O, ester), 1675 (C=O, carboxylic), 1654 (C=O, amide), 1576 (C=C), 1491 (C=C), 1307 ($\text{C}_{\text{Ar}}\text{-N}$), 1101 (C-O), 945, 848, 785 (1,2,4-trisubstituted benzene), 741 (C-H bending), 650 (C-H rocking); ^1H NMR (500 MHz, $\text{DMSO}-d_6$) δ 12.14 (s, 1 H, COOH), 10.47 (s, 1 H, NH), 8.12 (d, $J = 8.7$ Hz, 1 H, Ar-H), 7.87 (d, $J = 2.2$ Hz, 1 H, Ar-H), 7.65 (dd, $J = 8.7, 2.2$ Hz, 1 H, Ar-H), 3.84 (s, 3 H, OCH_3), 2.60 (t, $J = 6.2$ Hz, 2 H, CH_2), 2.50 (t, $J = 6.2$ Hz, 2 H, CH_2), 2.38 (s, 3 H, SeCH_3); ^{13}C NMR (126 MHz, $\text{DMSO}-d_6$) δ 173.44, 170.11, 166.89, 137.51, 135.23, 131.34, 125.06, 121.98, 118.84, 52.39, 31.59, 28.68, 7.07. MS (ESI): $m/z = \text{found } 368.1 [\text{M}^+ + \text{Na}]$; calcd. 368.0 [$\text{M}^+ + \text{Na}$]. $\text{C}_{13}\text{H}_{15}\text{NO}_5\text{Se}$ (345.01) C, 45.36; H, 4.39; N, 4.07. Found C, 45.39; H, 4.40; N, 4.05.

3.2.3. Synthesis of (Z)-4-((2-(Methoxycarbonyl)-4-(Methylselanyl)Phenyl)Amino)-4-Oxobut-2-Enoic Acid (**9**)

Compound **9** was obtained from methyl 2-amino-5-(benzylselanyl)benzoate (**5**) (1.0 mmol, 321 mg) and maleic anhydride (1.3 mmol, 127 mg). The reaction was followed by TLC (CH₂Cl₂/methanol 5%; R_f = 0.29), isolated as a yellow solid with 72% yield (302 mg), and its m.p. = 130–131 °C. IR (FT-IR, cm⁻¹): 3253 (NH), 3191 (broad O-H, carboxylic acid), 3027 (C_{Ar}-H), 2907 (C_{aliph}-H) 1708 (C=O, ester), 1625 (C=O, carboxylic), 1594 (C=O, amide), 1571, 1490 (C=C), 1297(C_{Ar}-N), 1243, 1040 (C-O), 954, 848, 823 (1,2,4-trisubstituted benzene), 785, 764 (C-H rocking), 750, 741 (C-H bending), 690 (monosubstituted benzene); ¹H NMR (500 MHz, DMSO-d₆) δ 12.98 (s, 1 H, COOH), 10.73 (s, 1 H, NH), 8.14 (d, J = 8.6 Hz, 1 H, Ar-H), 7.87 (d, J = 2.1 Hz, 1 H, Ar-H), 7.70 (dd, J = 8.6, 2.1 Hz, 1 H, Ar-H), 7.29–7.22 (m, 4 H, Ar-H), 7.21–7.15 (m, 1 H, Ar-H), 6.54 (d, J = 12.4 Hz, 1 H, =CH₂), 6.32 (d, J = 12.4 Hz, 1 H, CH₂=), 4.26 (s, 2 H, SeCH₂Ph), 3.82 (s, 3 H, OCH₃); ¹³C NMR (126 MHz, DMSO-d₆) δ 166.66, 166.50, 163.35, 138.40, 137.97, 137.75, 134.38, 132.13, 129.97, 128.76, 128.21, 126.70, 124.26, 121.93, 118.78, 52.44, 31.10. MS (ESI): *m/z* = found 442.1 [M⁺ + Na]; calcd. 442.0 [M⁺ + Na]. C₁₉H₁₇NO₅Se (419.03) C, 54.55; H, 4.10; N, 3.35. Found C, 54.52; H, 4.12; N, 3.34.

3.2.4. Synthesis of 4-((2-(Methoxycarbonyl)-4-(Methylselanyl)Phenyl)Amino)-4-Oxobut-2-Enoic Acid (**10**)

Compound **10** was obtained from methyl 2-amino-5-(benzylselanyl)benzoate (**5**) (1.0 mmol, 321 mg), and succinic anhydride (1.3 mmol, 130 mg). The reaction was followed by TLC (CH₂Cl₂/methanol 5%; R_f = 0.34) and isolated as a yellow solid with 41% yield (189 mg), and its m.p. = 145–146 °C. IR (FT-IR, cm⁻¹): 3264 (NH), 3200 (broad O-H, carboxylic acid), 3083 (C_{Ar}-H), 2945, 2841 (C_{aliph}-H), 1687 (C=O, ester), 1672 (C=O, carboxylic), 1592 (C=O, amide), 1579, 1508 (C=C), 1305 (C_{Ar}-N), 1291 (C_{Ar}-N), 1225, 1100 (C-O), 920, 848, 791 (1,2,4-trisubstituted benzene), 764 (C-H bending), 700 (monosubstituted benzene); ¹H NMR (500 MHz, DMSO-d₆) δ 12.17 (s, 1 H, COOH), 10.54 (s, 1 H, NH), 8.14 (d, J = 8.6 Hz, 1 H, Ar-H), 7.84 (dd, J = 8.6, 2.0 Hz, 1 H, Ar-H), 7.66 (dd, J = 8.6, 2.1 Hz, 1 H, Ar-H), 7.28–7.11 (m, 5 H, Ar-H), 4.22 (s, 2 H, SeCH₂Ph), 3.83 (s, 3 H, OCH₃), 2.61 (t, J = 6.4 Hz, 2 H, CH₂), 2.53 (t, J = 6.7 Hz, 2 H, CH₂); ¹³C NMR (126 MHz, DMSO-d₆) δ 173.41, 170.19, 166.83, 138.58, 138.46, 138.24, 134.61, 128.73, 128.17, 126.64, 123.08, 121.45, 118.09, 52.35, 31.67, 31.16, 28.58. MS (ESI): *m/z* = found 420.2 [M⁺ - H], 444.0 [M⁺ + Na]; calcd. 444.0 [M⁺ + Na]. C₁₉H₁₉NO₅Se (421.00) C, 54.29; H, 4.56; N, 3.33. Found C, 54.30; H, 4.57; N, 3.32.

3.2.5. Synthesis of (Z)-4-((2-(Methoxycarbonyl)-4-(Methylselanyl)Phenyl)Amino)-4-Oxobut-2-Enoic Acid (**11**)

Compound **11** was obtained from methyl 2-amino-5-((2-oxo-2-(phenylamino)ethyl)selanyl)benzoate (**6**) (1.0 mmol, 364 mg) and maleic anhydride (1.3 mmol, 127 mg). The reaction was followed by TLC (CH₂Cl₂/methanol 5%; R_f = 0.31), isolated as a yellow solid with 95% yield (439 mg), and its m.p. = 175–176 °C. IR (FT-IR, cm⁻¹): 3250 (NH), 3190 (NH), 3058 (C_{Ar}H), 2984, 2969 (C_{aliph}-H), 1716 (C=O, ester), 1706 (C=O, carboxylic), 1653 (C=O, amide), 1595, 1572 (C=C), 1528 (C=C), 1321 (C_{Ar}-N), 1297 (C_{Ar}-N), 1102 (C-O), 954, 841, 824 (1,2,4-trisubstituted benzene), 760, 700 (monosubstituted benzene), 680 (C-H bending); ¹H NMR (500 MHz, DMSO-d₆) δ 10.75 (s, 1 H, COOH), 10.10 (s, 1 H, NH), 8.15 (d, J = 8.6 Hz, 1 H, Ar-H), 8.06 (t, J = 7.0 Hz, 1 H, Ar-H), 7.84 (dd, J = 8.6, 2.1 Hz, 1 H, Ar-H), 7.51 (dd, J = 8.5, 1.0 Hz, 2 H, Ar-H), 7.31–7.26 (m, 2 H, Ar-H), 7.04 (dd, J = 8.5, 2.2 Hz, 1 H, Ar-H), 6.59 (d, J = 8.5 Hz, 1 H, CH=), 6.36 (d, J = 8.5 Hz, 1 H, =CH), 3.78 (s, 3 H, OCH₃), 3.74 (s, CH₂), 3.72 (s, 1 H, NH); ¹³C NMR (126 MHz, DMSO-d₆) δ 167.66, 166.63, 166.49, 163.38, 138.78, 137.93, 134.43, 132.13, 129.98, 128.62, 128.53, 123.92, 123.29, 122.04, 119.00, 117.30, 52.43, 30.77. MS (ESI): *m/z* = found 461.3 [M⁺ - H], 462.0 [M⁺], 485.2 [M⁺ + Na]; calcd. 462.0 [M⁺]. C₂₀H₁₈N₂O₆Se (462.03) C, 52.07; H, 3.93; N, 6.07. Found C, 52.10; H, 3.92; N, 6.08.

3.2.6. Synthesis of 4-((2-(Methoxycarbonyl)-4-(Methylselanyl)Phenyl)Amino)-4-Oxobut-2-enoic Acid (**12**)

Compound **12** was obtained from methyl 2-amino-5-((2-oxo-2-(phenylamino)ethyl)selanyl)benzoate (**6**) (1.0 mmol, 364 mg) and succinic anhydride (1.3 mmol, 130 mg). The reaction was followed by TLC (CH₂Cl₂/methanol 5%; R_f = 0.35) and isolated as a yellow solid with 79% yield (366 mg), and its m.p. = 127–128 °C. IR (FT-IR, cm⁻¹): 3313 (NH), 3279 (broad O-H, carboxylic acid), 3058 (C_{Ar}-H), 2949, 2859 (C_{aliph}-H), 1706 (C=O, ester), 1681 (C=O, carboxylic), 1648 (C=O, amide), 1597 (C=O, amide), 1577 (C=C), 1532 (C=C), 1508 (C=C), 1499 (CO), 1306 (C_{Ar}-N), 1251 (C_{Ar}-N), 1227 (C-O), 1173 (C-O), 971, 842, 789 (1,2,4-trisubstituted benzene), 760, 694 (monosubstituted benzene); ¹H NMR (500 MHz, DMSO-d₆) δ 12.14 (s, 1 H, COOH), 10.56 (s, 1 H, NH), 8.16 (d, J = 8.6 Hz, 1 H, Ar-H), 8.05 (d, J = 2.1 Hz, 1 H, Ar-H), 7.80 (dd, J = 8.6, 2.1 Hz, 1 H, Ar-H), 7.40–7.60 (m, 3 H, Ar-H), 7.03 (dd, J = 8.5, 2.2 Hz, 2 H, Ar-H), 3.79 (s, 3 H, OCH₃), 3.72 (s, 2 H, CH₂), 2.62 (t, J = 6.6 Hz, 2 H, CH₂), 2.53 (t, J = 6.6 Hz, 2 H, CH₂); ¹³C NMR (126 MHz, DMSO-d₆) δ 173.57, 170.38, 167.81, 166.97, 151.34, 140.63, 138.30, 137.68, 134.77, 128.69, 123.28, 119.15, 117.45, 52.51, 31.89, 30.99, 28.76; MS (ESI): *m/z* = found 463.3 [M⁺ - H], 487.2 [M⁺ + Na]; calcd. 464.0 [M⁺]. C₂₀H₂₀N₂O₆Se (464.05) C, 51.84; H, 4.35; N, 6.05. Found C, 51.80; H, 4.34; N, 6.04.

3.3. Computational Calculations

3.3.1. DFT Calculations

The compounds' geometries were optimized using the DFT/B3LYP [66–68] method with the 6-311G (d,p) basis set [69–71], which was implemented in the Gaussian 09w [72]. The energies of both the highest occupied molecular orbital (HOMO) and the lowest unoccupied molecular orbital (LUMO) were used to evaluate the following parameters: energy gap ($\Delta E = E_{\text{LUMO}} - E_{\text{HOMO}}$), electron affinity (E.A. = $-E_{\text{LUMO}}$), ionization potential (I.P. = $-E_{\text{HOMO}}$), electronegativity ($\chi = (\text{I.P.} + \text{E.A.})/2$), chemical potential ($\text{cp} = -\chi$), chemical hardness ($\eta = (\text{I.P.} - \text{E.A.})/2$), softness ($\sigma = 1/\eta$), and electrophilicity index ($\omega = \chi^2/2\eta$) [73,74].

3.3.2. Molecular Docking Investigation

The titled compounds were used as ligands (substrates) for investigation of their binding ability towards SARS-CoV-2 M^{Pro} (PDB: 7BFB) [75] through a molecular docking approach and using MOE to confirm their therapeutic behavior [76]. Additionally, the compounds were used as ligands (substrates) for investigation of their binding ability towards SARS-CoV-2 M^{Pro} (PDB ID: 6LU7) [18].

For ligand preparation, the optimized structures (by DFT) of the target compounds were used as the input to MOE and used as ligands for the molecular docking investigation. Finally, the obtained database was then saved as an MDB file to be used in the docking calculations [77,78].

For the protein and its active site preparation, the X-ray crystallographic structures of the SARS-CoV-2 M^{Pro} complex (PDB: 7BFB) and SARS-CoV-2 M^{Pro} one (PDB ID: 6LU7) were downloaded from the Protein Data Bank database (<https://www.rcsb.org/>, accessed on 7 July 2023). Water and ions were removed from the PDB file. The active site was chosen to contain the co-crystallized inhibitor (Co) bound to the active site of the receptor. For the 7BFB, the original ligand was extracted and the new ligands fitted into the binding pocket of 7BFB after defining Cys44 as the binding site [75,79].

For the docking process, the docking investigations were performed to assess the binding free energy of the inhibitor (ligand) inside the macromolecule (target protein receptor). The scoring in docking studies was conducted utilizing the London dG scoring function. Each docking experiment was derived from 100 different runs that were directed to analyze and achieve the best score. The docking patterns and interaction parameters were exported to evaluate the interaction features and rank the inhibition activity based on score function (S, kcal/mol) [80].

3.4. Drug Likeness and ADMET Prediction

Computer-based evaluations of ADMET (absorption, distribution, metabolism, excretion, and toxicity) properties are widely used in drug development. Tools such as pkCSM [56,81] and SwissADME [55,82] were utilized to predict ADMET and the drug-likeness of drug candidate molecules. These tools assess properties such as absorption (including gastrointestinal absorption, bioavailability, water solubility (log S), Caco-2, and skin permeability), distribution (including blood–brain barrier (BBB) and central nervous system (CNS) permeability and volume of distribution (VDss) in the unbound state), metabolism (including various metabolic enzymes of Cytochromes P450 (CYP)), excretion (including drug and renal clearance), and toxicity (including AMES and acute and chronic toxicity). These toxicological predictions were also used to apply the Lipinski rule and calculate bioavailability scores [83].

3.5. Molecular Dynamics (MD) Simulations

Both the MD simulations and the molecular mechanics generalized Born surface area (MM-GBSA) calculations [84,85] were carried out using the Desmond package of Schrödinger LLC [86,87]. The complete steps were described in the supplementary data (SI.1 and SI.2).

4. Conclusions

Novel OSe-based amidic acids (**7–12**) were delivered in excellent yields (up to 95%). Their chemical identities and electronic attributes were assessed using various spectroscopic techniques including DFT, MEOP, frontier molecular orbital, and ADMET analysis. The HOMO–LUMO energy gap enabled the calculation of the molecules' characteristics linked to their reactivity. The drug-likeness computations confirmed that the Lipinski rule was followed, and it was discovered that the compounds had good absorption, distribution, metabolism, and excretion rates overall. Moreover, the bioactivity of the new compounds was validated by using molecular docking towards the molecular target SARS-CoV-2 M^{PTO} (PDB: 7BFB). The novel molecules were found to attach to the leftover amino acids via various hydrophobic interactions and hydrogen bonds. Furthermore, MD simulations revealed that the behavior of compound **12** within the binding site of SARS-CoV-2 M^{PTO} was superior to its reference Co, indicating a very promising inhibition for the M^{PTO} of SARS-CoV-2. Moreover, MM-GBSA calculations clarified that compound **12** achieved a greatly superior ΔG binding energy (-59.07 kcal/mol) compared with the reference Co (-47.53 kcal/mol). The present *in silico* study proposed the potential SARS-CoV-2 inhibitory activity of the newly synthesized OSe candidates, which needs more advanced preclinical and clinical confirmations.

Supplementary Materials: The following supporting information can be downloaded at: <https://www.mdpi.com/article/10.3390/inorganics11080321/s1>, Figure S1: Various possible conformers of the title compounds; Figure S2: The plot of Natural charges distribution of the compounds **7–12** using the B3LYP/6-311G(d,p) in the gas phase; Figure S3: (a): The 3D structure of the 6lu7 of novel coronavirus (COVID-19); (b): Active site pocket in which molecular docking occurred; and (c) 3D and 2D interactions of the titled compounds inside the active site of the target receptor; Table S1: Drug Likeness parameters; Table S2: Pharmacokinetics, toxicities and receptor binding properties of potential bioactive compounds from medicinal plants using pkCSM web server; Table S3: Molecular Docking data; Interaction type, and distance between ligand and receptor of the title compounds. References [88,89] are related to the supplementary data.

Author Contributions: Data curation, S.S., A.A., H.B.-G., A.A.A.-K. and M.A.; Formal analysis, A.A., M.A., A.A.A.-K. and S.S.; Funding acquisition, G.M.A., Y.S.A.-F. and N.A.; Investigation, S.S., A.A. and M.A.; Methodology, S.S., A.A. and M.A.; Project administration, S.S., G.M.A., Y.S.A.-F. and N.A.; Resources, G.M.A., Y.S.A.-F., N.A. and A.A.; Supervision, S.S., A.A., M.A., G.M.A., Y.S.A.-F. and N.A.; Writing—original draft, S.S., A.A. and A.A.A.-K.; Writing—review and editing, S.S. and A.A. All authors have read and agreed to the published version of the manuscript.

Funding: The authors extend their appreciation to the Deputyship for Research and Innovation, Ministry of Education in Saudi Arabia for funding this research work (Project number INST134).

Institutional Review Board Statement: Not applicable.

Informed Consent Statement: Not applicable.

Data Availability Statement: The raw/processed data generated in this work are available upon request from the corresponding author.

Acknowledgments: The authors extend their appreciation to the Deputyship for Research and Innovation, Ministry of Education in Saudi Arabia for funding this research work (Project number INST134).

Conflicts of Interest: The authors declare no conflict of interest.

References

1. Radomska, D.; Czarnomysy, R.; Radomski, D.; Bielawska, A.; Bielawski, K. Selenium as a Bioactive Micronutrient in the Human Diet and Its Cancer Chemopreventive Activity. *Nutrients* **2021**, *13*, 1649. [[CrossRef](#)] [[PubMed](#)]
2. Schomburg, L. The other view: The trace element selenium as a micronutrient in thyroid disease, diabetes, and beyond. *Hormones* **2020**, *19*, 15–24. [[PubMed](#)]
3. Saleem, U.; Sabir, S.; Niazi, S.G.; Naeem, M.; Ahmad, B. Role of Oxidative Stress and Antioxidant Defense Biomarkers in Neurodegenerative Diseases. *Crit. Rev. Eukaryot. Gene Expr.* **2020**, *30*, 311–322. [[CrossRef](#)] [[PubMed](#)]
4. Bevinakoppamath, S.; Saleh Ahmed, A.M.; Ramachandra, S.C.; Vishwanath, P.; Prashant, A. Chemopreventive and Anticancer Property of Selenoproteins in Obese Breast Cancer. *Front. Pharmacol.* **2021**, *12*, 618172. [[CrossRef](#)]
5. Shaaban, S.; El-Lateef, H.M.A.; Khalaf, M.M.; Gouda, M.; Youssef, I. One-Pot Multicomponent Polymerization, Metal-, and Non-Metal-Catalyzed Synthesis of Organoselenium Compounds. *Polymers* **2022**, *14*, 2208. [[CrossRef](#)]
6. Arora, A.; Oswal, P.; Kumar Rao, G.; Kumar, S.; Kumar, A. Organoselenium ligands for heterogeneous and nanocatalytic systems: Development and applications. *Dalton Trans.* **2021**, *50*, 8628–8656. [[CrossRef](#)]
7. Phadnis, P.P. Synthesis Strategies for Organoselenium Compounds and Their Potential Applications in Human Life. In *Handbook on Synthesis Strategies for Advanced Materials*; Springer: Berlin/Heidelberg, Germany, 2021; pp. 537–641.
8. Pons, D.G.; Moran, C.; Alorda-Clara, M.; Oliver, J.; Roca, P.; Sastre-Serra, J. Micronutrients Selenomethionine and Selenocysteine Modulate the Redox Status of MCF-7 Breast Cancer Cells. *Nutrients* **2020**, *12*, 865. [[CrossRef](#)]
9. Wang, L.; Yang, Z.; Fu, J.; Yin, H.; Xiong, K.; Tan, Q.; Jin, H.; Li, J.; Wang, T.; Tang, W.; et al. Ethaselen: A potent mammalian thioredoxin reductase 1 inhibitor and novel organoselenium anticancer agent. *Free Radic. Biol. Med.* **2012**, *52*, 898–908. [[CrossRef](#)]
10. Benelli, J.L.; Poester, V.R.; Munhoz, L.S.; Melo, A.M.; Trápaga, M.R.; Stevens, D.A.; Xavier, M.O. Ebselen and diphenyl diselenide against fungal pathogens: A systematic review. *Med. Mycol.* **2021**, *59*, 409–421. [[CrossRef](#)]
11. Sies, H.; Parnham, M.J. Potential therapeutic use of ebselen for COVID-19 and other respiratory viral infections. *Free Radic. Biol. Med.* **2020**, *156*, 107–112. [[CrossRef](#)]
12. Harrison, N.L.; Sachs, J.D. A call for an independent inquiry into the origin of the SARS-CoV-2 virus. *Proc. Natl. Acad. Sci. USA* **2022**, *119*, e2202769119. [[CrossRef](#)] [[PubMed](#)]
13. Sancineto, L.; Ostacolo, C.; Ortega-Alarcon, D.; Jimenez-Alesanco, A.; Ceballos-Laita, L.; Vega, S.; Abian, O.; Velazquez-Campoy, A.; Moretti, S.; Dabrowska, A. L-arginine improves solubility and ANTI SARS-CoV-2 Mpro activity of Rutin but not the antiviral activity in cells. *Molecules* **2021**, *26*, 6062. [[PubMed](#)]
14. Xu, Z.; Yang, L.; Zhang, X.; Zhang, Q.; Yang, Z.; Liu, Y.; Wei, S.; Liu, W. Discovery of potential flavonoid inhibitors against COVID-19 3CL proteinase based on virtual screening strategy. *Front. Mol. Biosci.* **2020**, *7*, 556481.
15. Ampornanai, K.; Meng, X.; Shang, W.; Jin, Z.; Rogers, M.; Zhao, Y.; Rao, Z.; Liu, Z.-J.; Yang, H.; Zhang, L. Inhibition mechanism of SARS-CoV-2 main protease by ebselen and its derivatives. *Nat. Commun.* **2021**, *12*, 3061. [[CrossRef](#)]
16. La Monica, G.; Bono, A.; Lauria, A.; Martorana, A. Targeting SARS-CoV-2 main protease for treatment of COVID-19: Covalent inhibitors structure–activity relationship insights and evolution perspectives. *J. Med. Chem.* **2022**, *65*, 12500–12534.
17. Shivakoti, R.; Gupte, N.; Yang, W.-T.; Mwelase, N.; Kanyama, C.; Tang, A.M.; Pillay, S.; Samaneka, W.; Riviere, C.; Berendes, S. Pre-antiretroviral therapy serum selenium concentrations predict WHO stages 3, 4 or death but not virologic failure post-antiretroviral therapy. *Nutrients* **2014**, *6*, 5061–5078. [[CrossRef](#)] [[PubMed](#)]
18. Jin, Z.; Du, X.; Xu, Y.; Deng, Y.; Liu, M.; Zhao, Y.; Zhang, B.; Li, X.; Zhang, L.; Peng, C. Structure of Mpro from SARS-CoV-2 and discovery of its inhibitors. *Nature* **2020**, *7811*, 289–293. [[CrossRef](#)]
19. Wang, K.Y.; Liu, F.; Jiang, R.; Yang, X.; You, T.; Liu, X.; Xiao, C.Q.; Shi, Z.; Jiang, H.; Rao, Z. Structure of Mpro from COVID-19 virus and discovery of its inhibitors. *Nature* **2020**, *582*, 289–293.
20. Li, Q.; Kang, C. Progress in developing inhibitors of SARS-CoV-2 3C-like protease. *Microorganisms* **2020**, *8*, 1250.
21. Jin, Z.; Zhao, Y.; Sun, Y.; Zhang, B.; Wang, H.; Wu, Y.; Zhu, Y.; Zhu, C.; Hu, T.; Du, X. Structural basis for the inhibition of SARS-CoV-2 main protease by antineoplastic drug carmofur. *Nat. Struct. Mol. Biol.* **2020**, *27*, 529–532.

22. Weglarz-Tomczak, E.; Tomczak, J.M.; Talma, M.; Burda-Grabowska, M.; Giurg, M.; Brul, S. Identification of ebselen and its analogues as potent covalent inhibitors of papain-like protease from SARS-CoV-2. *Sci. Rep.* **2021**, *11*, 3640. [[CrossRef](#)]
23. Alotaibi, J.S.; Al-Faiyz, Y.S.; Shaaban, S. Design, Synthesis, and Biological Evaluation of Novel Hydroxamic Acid-Based Organoselenium Hybrids. *Pharmaceuticals* **2023**, *16*, 367–383. [[CrossRef](#)] [[PubMed](#)]
24. Shaaban, S.; Abdou, A.; Alhamzani, A.G.; Abou-Krishna, M.M.; Al-Qudah, M.A.; Alaasar, M.; Youssef, I.; Yousef, T.A. Synthesis and in silico investigation of organoselenium-clubbed schiff bases as potential M^{Pro} inhibitors for the SARS-CoV-2 replication. *Life* **2023**, *13*, 912–939. [[CrossRef](#)] [[PubMed](#)]
25. Menéndez, C.A.; Byléhn, F.; Perez-Lemus, G.R.; Alvarado, W.; de Pablo, J.J. Molecular characterization of ebselen binding activity to SARS-CoV-2 main protease. *Sci. Adv.* **2020**, *6*, eabd0345. [[CrossRef](#)]
26. Alaasar, M. Unexpected Kinetically Controlled Organoselenium-Based Isomaleimide: X-Ray Structure, Hirshfeld Surface Analysis, 3D Energy Framework Approach, and DFT Calculation. *Front. Chem.* **2022**, *10*, 879.
27. Haval, K.P.; Mhaske, S.B.; Argade, N.P. Cyanuric chloride: Decent dehydrating agent for an exclusive and efficient synthesis of kinetically controlled isomaleimides. *Tetrahedron* **2006**, *62*, 937–942. [[CrossRef](#)]
28. Tonglairoum, P.; Brannigan, R.P.; Opanasopit, P.; Khutoryanskiy, V.V. Maleimide-bearing nanogels as novel mucoadhesive materials for drug delivery. *J. Mater. Chem. B* **2016**, *4*, 6581–6587. [[CrossRef](#)]
29. Viveki, A.B.; Pol, M.D.; Halder, P.; Sonavane, S.R.; Mhaske, S.B. Annulation of Enals with Carbamoylpropiolates via NHC-Catalyzed Enolate Pathway: Access to Functionalized Maleimides/Iso-maleimides and Synthesis of Aspergillus FH-X-213. *J. Org. Chem.* **2021**, *86*, 9466–9477. [[CrossRef](#)] [[PubMed](#)]
30. Ravasco, J.M.; Faustino, H.; Trindade, A.; Gois, P.M. Bioconjugation with maleimides: A useful tool for chemical biology. *Chem. –A Eur. J.* **2019**, *25*, 43–59. [[CrossRef](#)] [[PubMed](#)]
31. Shaaban, S.; Vervandier-Fasseur, D.; Andreoletti, P.; Zarrouk, A.; Richard, P.; Negm, A.; Manolikakes, G.; Jacob, C.; Cherkaoui-Malki, M. Cytoprotective and antioxidant properties of organic selenides for the myelin-forming cells, oligodendrocytes. *Bioorganic Chem.* **2018**, *80*, 43–56.
32. Al-Abdallah, B.; Al-Faiyz, Y.S.; Shaaban, S. Organoselenocyanates Tethered Methyl Anthranilate Hybrids with Promising Anticancer, Antimicrobial, and Antioxidant Activities. *Inorganics* **2022**, *10*, 246. [[CrossRef](#)]
33. Zhang, L.; Hao, G.F.; Tan, Y.; Xi, Z.; Huang, M.Z.; Yang, G.F. Bioactive conformation analysis of cyclic imides as protoporphyrinogen oxidase inhibitor by combining DFT calculations, QSAR and molecular dynamic simulations. *Bioorganic Med. Chem.* **2009**, *17*, 4935–4942. [[CrossRef](#)] [[PubMed](#)]
34. Hossain, M.; Khushy, K.; Latif, M.; Hossen, M.F.; Asraf, M.A.; Kudrat-E-Zahan, M.; Abdou, A. Co (II), Ni (II), and Cu (II) Complexes Containing Isatin-Based Schiff Base Ligand: Synthesis, Physicochemical Characterization, DFT Calculations, Antibacterial Activity, and Molecular Docking Analysis. *Russ. J. General. Chem.* **2022**, *92*, 2723–2733.
35. Pokharia, S.; Joshi, R.; Pokharia, M.; Yadav, S.K.; Mishra, H. A density functional theory insight into the structure and reactivity of diphenyltin (IV) derivative of glycylphenylalanine. *Main. Group. Metal. Chem.* **2016**, *39*, 77–86. [[CrossRef](#)]
36. Singh, M.B.; Jain, P.; Tomar, J.; Kumar, V.; Bahadur, I.; Arya, D.K.; Singh, P. An In Silico investigation for acyclovir and its derivatives to fight the COVID-19: Molecular docking, DFT calculations, ADME and td-Molecular dynamics simulations. *J. Indian. Chem. Soc.* **2022**, *99*, 100433.
37. Fukui, K.; Yonezawa, T.; Shingu, H. A molecular orbital theory of reactivity in aromatic hydrocarbons. *J. Chem. Phys.* **1952**, *20*, 722–725. [[CrossRef](#)]
38. Fukui, K. Role of frontier orbitals in chemical reactions. *science* **1982**, *218*, 747–754. [[CrossRef](#)]
39. Houchi, S.; Messasma, Z. Exploring the inhibitory potential of Saussurea costus and Saussurea involucrata phytoconstituents against the Spike glycoprotein receptor binding domain of SARS-CoV-2 Delta (B. 1.617. 2) variant and the main protease (Mpro) as therapeutic candidates, using Molecular docking, DFT, and ADME/Tox studies. *J. Mol. Struct.* **2022**, *1263*, 133032. [[PubMed](#)]
40. Mohapatra, R.K.; Perekhoda, L.; Azam, M.; Suleiman, M.; Sarangi, A.K.; Semenets, A.; Pintilie, L.; Al-Resayes, S.I. Computational investigations of three main drugs and their comparison with synthesized compounds as potent inhibitors of SARS-CoV-2 main protease (Mpro): DFT, QSAR, molecular docking, and in silico toxicity analysis. *J. King Saud. Univ. -Sci.* **2021**, *33*, 101315.
41. Ghazy, A.; Hemeda, O.; Al-Hossainy, A.; Ghazy, R.; Henaish, A. Docking of COVID-19 Main Protease and TD-DFT/DMO13 Simulated method, Synthesis, and Characterization with hybrid nanocomposite thin films and its applications. *Surf. Interfaces* **2023**, *37*, 102722. [[CrossRef](#)]
42. Sagaama, A.; Brandan, S.A.; Issa, T.B.; Issaoui, N. Searching potential antiviral candidates for the treatment of the 2019 novel coronavirus based on DFT calculations and molecular docking. *Heliyon* **2020**, *6*, e04640. [[CrossRef](#)]
43. Guidara, S.; Ahmed, A.B.; Abid, Y.; Feki, H. Molecular structure, vibrational spectra and nonlinear optical properties of 2, 5-dimethylanilinium chloride monohydrate: A density functional theory approach. *Spectrochim. Acta Part. A Mol. Biomol. Spectrosc.* **2014**, *127*, 275–285.
44. Liu, C.; Luo, Y.; Lu, X.-B. DFT Studies on the Origin of Regioselective Ring-opening of Terminal Epoxides during Copolymerization with CO₂. *Chin. J. Polym. Sci.* **2016**, *34*, 439–445.
45. Reed, A.E.; Curtiss, L.A.; Weinhold, F. Intermolecular interactions from a natural bond orbital, donor-acceptor viewpoint. *Chem. Rev.* **1988**, *88*, 899–926.

46. Al-Wabli, R.I.; Resmi, K.; Mary, Y.S.; Panicker, C.Y.; Attia, M.I.; El-Emam, A.A.; Van Alsenoy, C. Vibrational spectroscopic studies, Fukui functions, HOMO-LUMO, NLO, NBO analysis and molecular docking study of (E)-1-(1, 3-benzodioxol-5-yl)-4, 4-dimethylpent-1-en-3-one, a potential precursor to bioactive agents. *J. Mol. Struct.* **2016**, *1123*, 375–383.
47. Chaudhary, A.P.; Bharti, S.K.; Kumar, S.; Ved, K.; Padam, K. Study of molecular structure, chemical reactivity and first hyperpolarizability of a newly synthesized N-(4-oxo-2-phenylquinazolin-3 (4H)-yl)-1H-indole-2-carboxamide using spectral analysis. *J. Mol. Struct.* **2017**, *1148*, 356–363.
48. Lipinski, C.A.; Lombardo, F.; Dominy, B.W.; Feeney, P.J. Experimental and computational approaches to estimate solubility and permeability in drug discovery and development settings. *Adv. Drug Deliv. Rev.* **2012**, *64*, 4–17. [[CrossRef](#)]
49. Martin, Y.C. A bioavailability score. *J. Med. Chem.* **2005**, *48*, 3164–3170. [[CrossRef](#)]
50. Al-Gaber, M.A.I.; Abd El-Lateef, H.M.; Khalaf, M.M.; Shaaban, S.; Shawky, M.; Mohamed, G.G.; Abdou, A.; Gouda, M.; Abu-Dief, A.M. Design, Synthesis, Spectroscopic Inspection, DFT and Molecular Docking Study of Metal Chelates Incorporating Azo Dye Ligand for Biological Evaluation. *Materials* **2023**, *16*, 897. [[CrossRef](#)] [[PubMed](#)]
51. Daina, A.; Michielin, O.; Zoete, V. SwissADME: A free web tool to evaluate pharmacokinetics, drug-likeness and medicinal chemistry friendliness of small molecules. *Sci. Rep.* **2017**, *7*, 42717.
52. Bodnar, M.; Szczygłowska, M.; Konieczka, P.; Namiesnik, J. Methods of selenium supplementation: Bioavailability and determination of selenium compounds. *Crit. Rev. Food Sci. Nutr.* **2016**, *56*, 36–55.
53. Levander, O.A.; Alfthan, G.; Arvilommi, H.; Gref, C.; Huttunen, J.; Kataja, M.; Koivistoinen, P.; Pikkarainen, J. Bioavailability of selenium to Finnish men as assessed by platelet glutathione peroxidase activity and other blood parameters. *Am. J. Clin. Nutr.* **1983**, *37*, 887–897. [[CrossRef](#)] [[PubMed](#)]
54. Ali, J.; Camilleri, P.; Brown, M.B.; Hutt, A.J.; Kirton, S.B. Revisiting the general solubility equation: In silico prediction of aqueous solubility incorporating the effect of topographical polar surface area. *J. Chem. Inf. Model.* **2012**, *52*, 420–428. [[PubMed](#)]
55. Shabaan, S.; Ba, L.A.; Abbas, M.; Burkholz, T.; Denkert, A.; Gohr, A.; Wessjohann, L.A.; Sasse, F.; Weber, W.; Jacob, C. Multicomponent reactions for the synthesis of multifunctional agents with activity against cancer cells. *Chem. Comm.* **2009**, *31*, 4702–4704. [[CrossRef](#)] [[PubMed](#)]
56. Pires, D.E.; Blundell, T.L.; Ascher, D.B. pkCSM: Predicting small-molecule pharmacokinetic and toxicity properties using graph-based signatures. *J. Med. Chem.* **2015**, *58*, 4066–4072. [[CrossRef](#)] [[PubMed](#)]
57. Dahlgren, D.; Lennernäs, H. Intestinal permeability and drug absorption: Predictive experimental, computational and in vivo approaches. *Pharmaceutics* **2019**, *11*, 411.
58. Zanger, U.M.; Schwab, M. Pharmacology & Therapeutics Cytochrome P450 enzymes in drug metabolism: Regulation of gene expression, enzyme activities, and impact of genetic variation. *Pharmacol. Ther.* **2013**, *138*, 103–141. [[PubMed](#)]
59. Horde, G.W.; Gupta, V. *Drug Clearance*; StatPearls Publishing: St. Petersburg, FL, USA, 2023. [[PubMed](#)]
60. Han, Y.; Zhang, J.; Hu, C.; Zhang, X.; Ma, B.; Zhang, P. In silico ADME and toxicity prediction of ceftazidime and its impurities. *Front Pharmacol.* **2019**, *10*, 434. [[CrossRef](#)]
61. Arafath, M.A.; Adam, F.; Ahamed, M.B.K.; Karim, M.R.; Uddin, M.N.; Yamin, B.M.; Abdou, A. Ni (II), Pd (II) and Pt (II) complexes with SNO-group thiosemicarbazone and DMSO: Synthesis, characterization, DFT, molecular docking and cytotoxicity. *J. Mol. Struct.* **2023**, *1278*, 134887.
62. Nagasundaram, N.; Padmasree, K.; Santhosh, S.; Vinoth, N.; Sedhu, N.; Lalitha, A. Ultrasound promoted synthesis of new azo fused dihydropyrano [2, 3-c] pyrazole derivatives: In vitro antimicrobial, anticancer, DFT, in silico ADMET and Molecular docking studies. *J. Mol. Struct.* **2022**, *1263*, 133091.
63. Elagawany, M.; Elmaaty, A.A.; Mostafa, A.; Abo Shama, N.M.; Santali, E.Y.; Elgendy, B.; Al-Karmalawy, A.A. Ligand-based design, synthesis, computational insights, and in vitro studies of novel N-(5-Nitrothiazol-2-yl)-carboxamido derivatives as potent inhibitors of SARS-CoV-2 main protease. *J. Enzym. Inhib. Med. Chem.* **2022**, *37*, 2112–2132.
64. Khalid, Z.; Khan, A.T.-A.; Alnajjar, R.; Santali, E.; Shakoori, A.R. In silico mutational analysis of ACE2 to check the susceptibility of lung cancer patients towards COVID-19. *Sci. Rep.* **2022**, *12*, 7798.
65. Sak, M.; Al-Faiyz, Y.S.; Elsayy, H.; Shaaban, S. Novel organoselenium redox modulators with potential anticancer, antimicrobial, and antioxidant activities. *Antioxidants* **2022**, *11*, 1231. [[PubMed](#)]
66. Becke, A.D. Density-functional exchange-energy approximation with correct asymptotic behavior. *Phys. Rev. A* **1988**, *38*, 3098.
67. Lee, C.; Yang, W.; Parr, R.G. Development of the Colle-Salvetti correlation-energy formula into a functional of the electron density. *Phys. Rev. B* **1988**, *37*, 785.
68. Raghavachari, K. Perspective on “Density functional thermochemistry. III. The role of exact exchange” Becke AD (1993) *J Chem Phys* 98: 5648–52. *Theor. Chem. Acc.* **2000**, *103*, 361–363.
69. Hay, P.J.; Wadt, W.R. Ab initio effective core potentials for molecular calculations. Potentials for the transition metal atoms Sc to Hg. *J. Chem. Phys.* **1985**, *82*, 270–283.
70. McLean, A.; Chandler, G. Contracted Gaussian basis sets for molecular calculations. I. Second row atoms, Z= 11–18. *J. Chem. Phys.* **1980**, *72*, 5639–5648.
71. Krishnan, R.; Binkley, J.S.; Seeger, R.; Pople, J.A. Self-consistent molecular orbital methods. XX. A basis set for correlated wave functions. *J. Chem. Phys.* **1980**, *72*, 650–654.
72. Tomberg, A. Gaussian 09w tutorial. *Introd. Comput. Chem. Using G09W Avogadro Softw.* **2013**, 1–36.

73. Abbas, G.; Irfan, A.; Ahmed, I.; Al-Zeidaneen, F.K.; Muthu, S.; Fuhr, O.; Thomas, R. Synthesis and investigation of anti-COVID19 ability of ferrocene Schiff base derivatives by quantum chemical and molecular docking. *J. Mol. Struct.* **2022**, *1253*, 132242. [CrossRef] [PubMed]
74. Oyenehin, O.E.; Ojo, N.D.; Ipinloju, N.; James, A.C.; Agbaffa, E.B. Investigation of corrosion inhibition potentials of some aminopyridine schiff bases using density functional theory and Monte Carlo simulation. *Chem. Afr.* **2022**, *5*, 319–332. [CrossRef]
75. Qiao, Z.; Wei, N.; Jin, L.; Zhang, H.; Luo, J.; Zhang, Y.; Wang, K. The Mpro structure-based modifications of ebsele derivatives for improved antiviral activity against SARS-CoV-2 virus. *Bioorganic Chem.* **2021**, *117*, 105455. [CrossRef]
76. Scholz, C.; Knorr, S.; Hamacher, K.; Schmidt, B. DOCKTITE—A Highly Versatile Step-by-Step Workflow for Covalent Docking and Virtual Screening in the Molecular Operating Environment. *J. Chem. Inf. Model.* **2015**, *55*, 398–406. [CrossRef] [PubMed]
77. Vilar, S.; Cozza, G.; Moro, S. Medicinal chemistry and the molecular operating environment (MOE): Application of QSAR and molecular docking to drug discovery. *Curr. Top. Med. Chem.* **2008**, *8*, 1555–1572. [PubMed]
78. Yunta, M.J. Docking and ligand binding affinity: Uses and pitfalls. *Am. J. Model. Optim.* **2016**, *4*, 74–114.
79. Antonopoulou, I.; Sapountzaki, E.; Rova, U.; Christakopoulos, P. Inhibition of the main protease of SARS-CoV-2 (Mpro) by repurposing/designing drug-like substances and utilizing nature's toolbox of bioactive compounds. *Comput. Struct. Biotechnol. J.* **2022**, *20*, 1306–1344. [CrossRef]
80. Alghuwainem, Y.A.; El-Lateef, H.M.A.; Khalaf, M.M.; Amer, A.A.; Abdelhamid, A.A.; Alzharani, A.A.; Alfarsi, A.; Shaaban, S.; Gouda, M.; Abdou, A. Synthesis, DFT, biological and molecular docking analysis of novel manganese (II), Iron (III), Cobalt (II), Nickel (II), and Copper (II) Chelate Complexes Ligated by 1-(4-Nitrophenylazo)-2-naphthol. *Int. J. Mol. Sci.* **2022**, *23*, 15614.
81. Azzam, K.A. SwissADME and pkCSM webservers predictors: An integrated online platform for accurate and comprehensive predictions for in silico ADME/T properties of artemisinin and its derivatives. *Kompleks. Ispolz. Miner. Syra Complex. Use Miner. Resour.* **2023**, *325*, 14–21.
82. Zoete, V.; Daina, A.; Bovigny, C.; Michielin, O. SwissSimilarity: A web tool for low to ultra high throughput ligand-based virtual screening. *J. Chem. Inf. Model.* **2016**, *56*, 1399–1404. [CrossRef]
83. Lipinski, C.A.; Lombardo, F.; Dominy, B.W.; Feeney, P.J. Experimental and computational approaches to estimate solubility and permeability in drug discovery and development settings. *Adv. Drug Deliv. Rev.* **1997**, *23*, 3–25. [CrossRef]
84. Shi, S.; Wang, Q.; Liu, S.; Qu, Z.; Li, K.; Geng, X.; Wang, T.; Gao, J. Characterization the performances of twofold resveratrol integrated compounds in binding with SIRT1 by molecular dynamics simulation and molecular mechanics/generalized born surface area (MM/GBSA) calculation. *Chem. Phys.* **2021**, *544*, 111108. [CrossRef]
85. El-Masry, R.M.; Al-Karmalawy, A.A.; Alnajjar, R.; Mahmoud, S.H.; Mostafa, A.; Kadry, H.H.; Abou-Seri, S.M.; Taher, A.T. Newly synthesized series of oxindole-oxadiazole conjugates as potential anti-SARS-CoV-2 agents: In silico and in vitro studies. *New J. Chem.* **2022**, *46*, 5078–5090.
86. Release, S. 3: Desmond Molecular Dynamics System, DE Shaw Research, Maestro-Desmond Interoperability Tools, Schrödinger, New York, NY, USA. 2017. Available online: <https://www.schrodinger.com/products/desmond#block-3767> (accessed on 7 July 2023).
87. Hammoud, M.M.; Khattab, M.; Abdel-Motaal, M.; Van der Eycken, J.; Alnajjar, R.; Abulkhair, H.; Al-Karmalawy, A.A. Synthesis, structural characterization, DFT calculations, molecular docking, and molecular dynamics simulations of a novel ferrocene derivative to unravel its potential antitumor activity. *J. Biomol. Struct. Dyn.* **2023**, *41*, 5199–5216.
88. Ezz Eldin, R.R.; Saleh, M.A.; Alotaibi, M.H.; Alsuair, R.K.; Alzahrani, Y.A.; Alshehri, F.A.; Mohamed, A.F.; Hafez, S.M.; Althoqapy, A.A.; Khirala, S.K.; et al. Ligand-based design and synthesis of N'-Benzyldiene-3,4-dimethoxybenzohydrazide derivatives as potential antimicrobial agents; evaluation by in vitro, in vivo, and in silico approaches with SAR studies. *J. Enzym. Inhib. Med. Chem.* **2022**, *37*, 1098–1119. [CrossRef] [PubMed]
89. Abo Elmaaty, A.; Eldehna, W.M.; Khattab, M.; Kutkat, O.; Alnajjar, R.; El-Taweel, A.N.; Al-Rashood, S.T.; Abourehab, M.A.; Binjubair, F.A.; Saleh, M.A.; et al. Anticoagulants as Potential SARS-CoV-2 Mpro Inhibitors for COVID-19 Patients: In Vitro, Molecular Docking, Molecular Dynamics, DFT, and SAR Studies. *Int. J. Mol. Sci.* **2022**, *23*, 12235. [PubMed]

Disclaimer/Publisher's Note: The statements, opinions and data contained in all publications are solely those of the individual author(s) and contributor(s) and not of MDPI and/or the editor(s). MDPI and/or the editor(s) disclaim responsibility for any injury to people or property resulting from any ideas, methods, instructions or products referred to in the content.